IOP Publishing Phys. Med. Biol. 68 (2023) 02TR02 https://doi.org/10.1088/1361-6560/aca4b7

Physics in Medicine & Biology

IPEM Institute of Physics and Engineering in Medicine

RECEIVED
28 March 2022

REVISED
22 August 2022

ACCEPTED FOR PUBLICATION
21 November 2022

PUBLISHED
18 January 2023

TOPICAL REVIEW

Ultra-high field MRI: parallel-transmit arrays and RF pulse design

Sydney N Williams[1], Paul McElhinney[1] and Shajan Gunamony[1,2,*]

[1] Imaging Centre of Excellence, University of Glasgow, Glasgow, United Kingdom
[2] MR CoilTech Limited, Glasgow, United Kingdom
[*] Author to whom any correspondence should be addressed.

E-mail: sydney.williams@glasgow.ac.uk and shajan.gunamony@glasgow.ac.uk

Keywords: radiofrequency (RF) coils, ultra-high field (UHF) magnetic resonance imaging (MRI), parallel transmission (pTx), electromagnetic (EM) fields, specific absorption rate (SAR)

Abstract

This paper reviews the field of multiple or parallel radiofrequency (RF) transmission for magnetic resonance imaging (MRI). Currently the use of ultra-high field (UHF) MRI at 7 tesla and above is gaining popularity, yet faces challenges with non-uniformity of the RF field and higher RF power deposition. Since its introduction in the early 2000s, parallel transmission (pTx) has been recognized as a powerful tool for accelerating spatially selective RF pulses and combating the challenges associated with RF inhomogeneity at UHF. We provide a survey of the types of dedicated RF coils used commonly for pTx and the important modeling of the coil behavior by electromagnetic (EM) field simulations. We also discuss the additional safety considerations involved with pTx such as the specific absorption rate (SAR) and how to manage them. We then describe the application of pTx with RF pulse design, including a practical guide to popular methods. Finally, we conclude with a description of the current and future prospects for pTx, particularly its potential for routine clinical use.

1. Introduction

Magnetic resonance imaging (MRI) plays a powerful role in modern healthcare as a non-invasive diagnostic tool. Unlike other imaging modalities such as nuclear medicine and x-ray computed tomography, MRI does not use ionizing radiation and offers excellent soft tissue contrast. In recent years, member countries of the Organisation for Economic Co-operation and Development have increased MRI scanner prevalence to over 16 per 100 000 people (OECD 2022) with the highest application of clinical exams taking place in the spine, brain, upper extremites, and lower extremities with usage of 26%, 25%, 11%, and 9%, respectively (Rinck 2018).

Until recently, only MRI scanners with a static magnetic field strength of up to 3T had the regulatory approval for clinical use. Since the late 1990s, however, ultra-high field (UHF, $\geqslant$ 7T) scanners with 7T and even higher static magnetic field strengths such as 8T, 9.4T and 10.5T have been used in neuroscience and clinical research (Robitaille *et al* 1998, Vaughan *et al* 2001, 2006, Sadeghi–Tarakameh *et al* 2020). Continuing with this trend, a whole body 11.7T MRI scanner has been commissioned at CEA Neurospin, Paris and even 14.1T magnets for human imaging are currently under consideration (Nowogrodzki 2018). The push towards increasing the B_0 field strength is mainly driven by the inherent supra-linear increase in signal-to-noise ratio (SNR) with respect to the strength of the static magnetic field (Hoult and Richards 1976, Pohmann *et al* 2016). The SNR increase at UHF enables higher imaging resolution as well as unique imaging contrasts and enhanced opportunities for applications such as functional MRI (fMRI), spectroscopy, and susceptibility-weighted imaging (SWI).

At the same time, there are challenges associated with UHF MRI: the increased radiofrequency (RF) power deposition in tissue, the worsening of susceptibility and other imaging artifacts, and the greater non-uniformity of the RF field (Kraff and Quick 2017). By far the most popular approach to improve RF field homogeneity at UHF is a form of MRI called *parallel transmission* or 'pTx' (Hoult 2000, Ibrahim *et al* 2000). Since it's introduction, the technical development of dedicated pTx RF coils, pTx safety studies, and pTx pulse design have been a major theme of UHF MRI research (Padormo *et al* 2016).

Following the tremendous progress that has been achieved in understanding and mitigating the challenges of UHF, 7T MRI scanners from two vendors have been granted FDA ('FDA Clears GE 7T MRI,' 2020) and FDA and CE approval ('FDA Clears First 7T MRI,' 2017). Currently, the approval for clinical use concerns single-transmit (sTx) mode for imaging of the head or the knee. Already, close to one hundred 7T or higher field scanners are operational, and the uptake of 7T scanners for clinical use has been increasing since the regulatory approval for 7T MRI (Barisano et al 2019).

The next logical step in this progression is the approval for clinical use of pTx technology because this is essential to overcome RF field non-uniformity and fully exploit the capability of ultra-high field MRI. In addition, a wide range of high-performance RF coil arrays are necessary to develop clinical applications and expand 7T MRI to body parts other than the brain.

The aim of this review paper is to introduce the various components involved with pTx at UHF. First, we will describe the challenges motivating the development of pTx at UHF and provide an overview of the design considerations of dedicated transmit array coils. We then discuss briefly the role of electromagnetic (EM) field simulations in the design of transmit arrays and the management of their safety. Next, we will review applications of pTx and provide a generalized framework for pTx pulse design. Finally, we end with a look towards the future of pTx MRI. Selected references on each topic have been provided for further reading.

2. RF Challenges at UHF

MRI is based on the physical principles of nuclear magnetic resonance (NMR), and requires dedicated hardware to generate EM fields within the bore of the MRI scanner and to receive RF signals from atomic nuclei within the human body. An RF coil is an essential component responsible for two crucial functions during an MRI examination. Firstly, a *transmit* coil generates a magnetic field (B_1^+) perpendicular to the static magnetic field (B_0). The pulsed RF energy applied through the transmit coil flips the net magnetization of the atomic nuclei perpendicular to its equilibrium along the direction of B_0 in a circular motion called precession. The precessing magnetization induces a signal on a *receive* coil, which is the MR signal processed by the scanner to generate the MR image. The abovementioned transmit and receive functions are either performed by the same coil or by two separate coils. These RF coils are known as transceiver (TxRx) coils and transmit-only receive-only (ToRo) coils, respectively. The EM field produced by the transmit coil is expected to be homogeneous to achieve constant excitation flip angle across the imaging volume. This is essential to produce a homogeneous image with uniform tissue contrast.

The RF coils are made of resonant circuits tuned to the Larmor frequency ω_0, which depends on the nucleus and the strength of the main magnetic field B_0,

$$\omega_0 = 2\pi\gamma B_0, \tag{1}$$

where γ is the gyromagnetic ratio. The most widely used atomic nucleus used in MRI is ^{1}H because it has the highest inherent NMR sensitivity and is abundant in the body in the form of H_2O. For ^{1}H, the resonance frequency is 42.58 MHz at 1 tesla.

The engineering difficulties as well as the fundamental physics challenges increase with field strength because of the higher Larmor frequency and the decrease in consequent wavelength which becomes comparable to body dimensions. For example, ^{1}H 7T RF coils are tuned to about 298 MHz and the corresponding RF wavelength in biological tissue is 12 cm, which is about half the largest dimension of the head. This results in subject-dependent spatial variations in the B_1^+ field produced by the RF coil and an inhomogeneous image. In fact, the associated fundamental physical problems of RF magnetic field penetration, RF amplitude and phase variations in biological tissue, increase in RF power deposition, and the power required to achieve a 90° pulse were recognized very early in the development of MRI (Bottomley and Andrew 1978), although this study limited the feasibility of MRI to 10 MHz.

However, imaging studies performed at a range of field strengths from 4T to 9.4T demonstrated that imaging could be performed at these field strengths and that the fundamental issues such as RF penetration (Robitaille et al 1998), and RF power requirements (Vaughan et al 2001) would not be staggering at UHF. Although measurements at frequencies up to 220 MHz demonstrate that the power absorbed in conductive tissue increases with the square of the operating frequency (Roschmann 1987), numerical calculations of absorbed power and specific absorption rate (SAR) between 200 and 400 MHz (and Smith 2001a, Ibrahim 2004) suggest that this increase is not as fast as predicted with low frequency approximations. Simulations and experiments provide evidence that dielectric effects in the head overwhelm eddy current shielding and RF penetration issues (Robitaille et al 2000, Vaughan et al 2001).

While image non-uniformities due to central brightening seen with volume coils at 4T was initially attributed to the presence of dielectric resonances (Bomsdorf et al 1988, Barfuss et al 1990), analytical calculations confirmed that the resonances are dampened at conductivity levels of human tissue, and the central

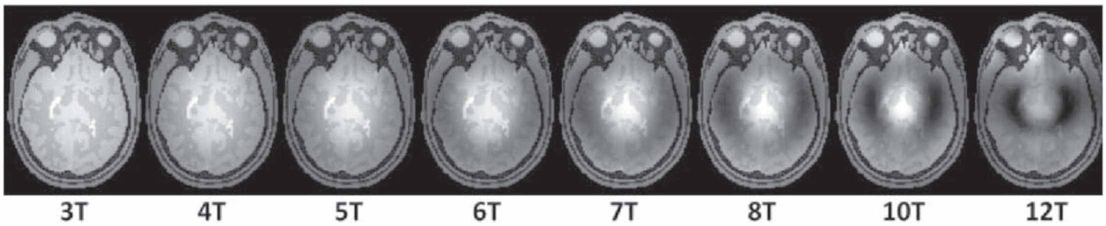

Figure 1. Demonstration of the effect of the reduced RF wavelength with increasing magnetic field strength via simulation of gradient-echo images. Reproduced with permission from Webb and Collins 2010. John Wiley & Sons. Copyright © 2010 Wiley Periodicals, Inc.

brightening is a field focusing effect (Hoult 2000). Subsequent theoretical and experimental studies at 8T demonstrated that dielectric resonance effects are not sustained at the permittivity and conductivity levels of the biological tissue (Ibrahim *et al* 2001a). The RF wave is attenuated at higher conductivities as it travels away from the coil and reflected from boundaries leading to a complex constructive and destructive interference pattern (Yang *et al* 2002, Van de Moortele *et al* 2005).

Figure 1 shows the progressively decreasing image homogeneity in simulation, which is caused by these constructive and destructive interference patterns due to RF wavelength effects in the human head for MRI field strengths ranging from to 3T to 12T (Webb and Collins 2010a). Due to the complex interactions between the RF coil and the sample, the spatial distribution of the B_1^+ field is determined by the geometry and electrical properties of the sample, the RF coil design itself as well as the amplitude and phase relationships between the input power to the coil elements (Adriany *et al* 2005).

In addition to the B_1^+ field inhomogeneity, the electric field produced by the RF coil, which generates electric currents in conductive tissue and causes tissue heating, plays an important role in UHF MRI. The RF power deposition in tissue is regulated by SAR, which is the absorbed RF power per tissue mass. SAR is calculated from the local electric field (E), local tissue conductivity (σ), and mass density (ρ) of tissue

$$\mathrm{SAR} = \frac{\sigma E^2}{2\rho}. \tag{2}$$

SAR is quantified by the global and local SAR in Watts per kilogram of tissue, and there are regulatory limits in terms of 10 s and time averaged over 6 min values ('IEC 60601-2-33,' 2010). Global SAR is the SAR averaged across entire body parts (whole body, partial-body, head) and local SAR is averaged over a volume of 10 g of tissue.

At static magnetic field strengths of up to 3T, the relationship between the applied RF power and energy deposition can be calculated by assuming a homogeneous RF field distribution. However, UHF MRI operates in the intermediate region between the near and far-field where the RF field distribution in biological tissue is a function of the subject size and position, and becomes proggessively more inhomogeneous (figure 1). This increases the risk of localized 'RF hot spots' due to elevated power deposition. Hence the concern is the increase in RF power deposition in the exposed anatomy yielding a rise in local temperature.

While SAR is used as a surrogate metric, temperature is the primary safety criterion. This is modelled by the Pennes bioheat equation (Pennes 1948, Le Ster 2021)

$$\rho c\frac{dT}{dt} = \nabla k \cdot \nabla T + k\nabla^2 T - B(T - T_b) + Q_m + \rho SAR. \tag{3}$$

Here, c is the tissue heat capacity, k is the thermal conductivity, T, is the absolute temperature, T_b, is the arterial blood temperature, B is the blood perfusion, and Q_m is the heat generated by metabolism. SAR and temperature distribution on similar types of coils at 3T and 7T exhibit very different spatial distribution (Webb and Collins 2010a). Therefore, full-wave EM field simulations which include heterogenous body models, create accurate numerical models of the RF coil, and capture the MRI scanner environment have played an improtant role in safety assessment and verification at UHF.

Thus, the major engineering challenge in the design of an RF coil for ultra-high field MRI is the ability to produce a strong and homogeneous B_1^+ field, while managing the RF power deposition and staying within the FDA or IEC SAR guidelines (Delfino 2014, 'IEC 60601-2-33,' 2010).

3. Parallel RF transmission

In clinical MRI scanners with static magnetic field strengths up to 3T, a large volume coil is installed in the scanner bore. A volume coil encompasses the anatomy of interest, and the most commonly used volume coil is

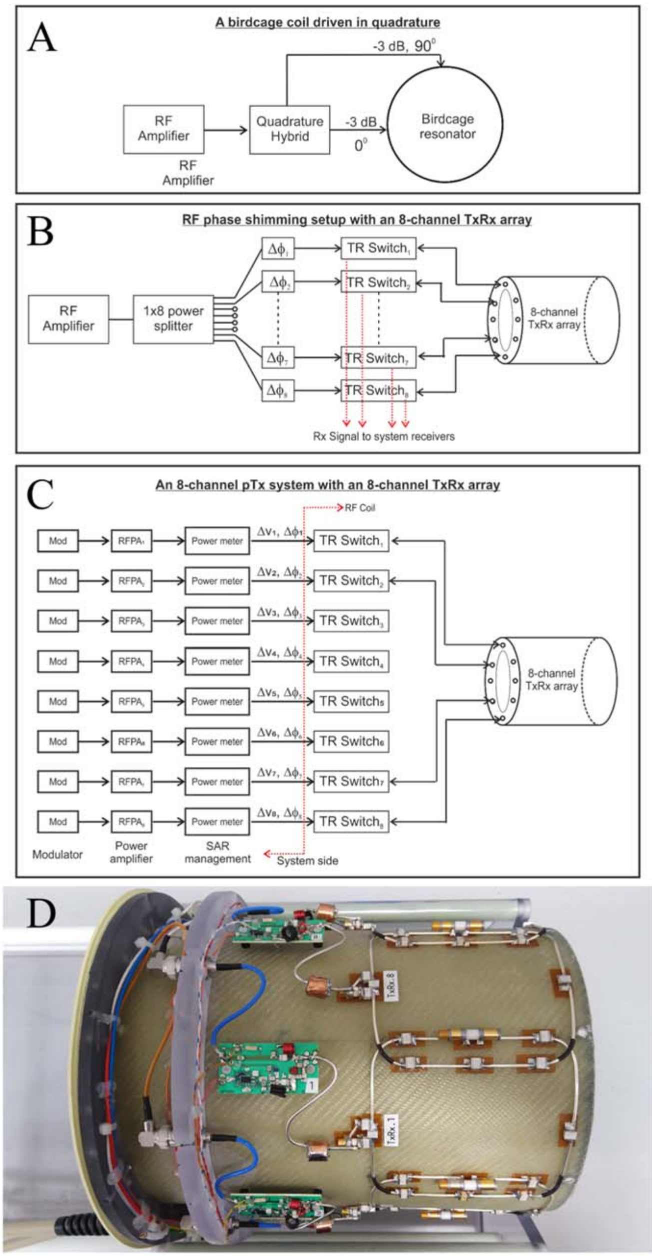

Figure 2. (A) Functional block diagram of a circularly polarized birdcage resonator. (B) A passive RF shimming setup consisting of a power splitter and an 8-channel TxRx array. The length of the coaxial cable between the power splitter and the coil input can be altered in this setup. (C) A dynamic pTx system which allows independent control of the amplitude and phase of the currents to the coil elements. (D) Photograph of an 8-channel TxRx array with built-in TR switches.

the birdcage resonator (Hayes *et al* 1985). The birdcage resonators installed in the MRI scanner bore are body-sized resonators capable of producing a homogeneous B_1^+ field over a large field of view (FOV) and are typically referred to as body coils.

The body coil is primarily operated as a transmit coil but can also be operated as a transmit-receive coil. The two orthogonal modes of the birdcage resonator are excited with an RF input of equal amplitude but with a 90° phase offset (Glover *et al* 1985) to set up a circularly polarized (CP) RF excitation. This is typically achieved by feeding the output of the RF power amplifier (RFPA) through a high-power quadrature hybrid to generate two outputs. Figure 2(A) shows a functional block diagram of this configuration.

The introduction of phased array technology by Roemer *et al* revolutionized MR signal detection and has resulted in tremendous advances towards improved sensitivity (Roemer *et al* 1990) and reduced scan time (Sodickson and Manning 1997, Pruessmann *et al* 1999, Griswold *et al* 2002) in MRI examinations. The phased array technology enabled simultaneous detection of MR signal with an array of surface coils, and outperforms a single large coil covering the same area. Shortly after, the phased array concept was extended to volume imaging (Hayes *et al* 1991). This work further demonstrated that the SNR of a receive array is significantly better than the large body coil. Dedicated receive array coils for the anatomy of interest thus became the most favored method of signal detection, with the built-in body coil being used as a transmit coil for spin excitation.

Body sized volume transmit coils analogous to those at field strengths of 1.5T and 3T are not feasible at UHF due to the B_1^+ field inhomogeneity already introduced in the previous section. The spatial distribution of the B_1^+ field produced by the coil, which is homogeneous in the absence of a load, becomes highly non-uniform when the coil is loaded with a human body (Vaughan *et al* 2001). The RF field interferences can cause total cancellation of the B_1^+ field as demonstrated in figure 1, when the transmit coil is excited in the conventional CP mode.

pTx was originally introduced in 2000 as a means of mitigating transmit RF field inhomogeneity (Hoult 2000, Ibrahim *et al* 2000). In pTx, a dedicated RF coil with multiple, independent channels generates individual B_1^+ fields. These single-channel fields enable a spatially varying combined B_1^+ field that can be optimized for homogeneous imaging even with the reduced RF wavelengths at UHF. Shortly afer, the concept of pTx RF pulses known as Transmit SENSE (Katscher *et al* 2003, Zhu 2004) was presented. This is analogous to the well known parallel imaging concept on the receive side, in which the undersampled data is reconstructed by leveraging the sensitivies of multiple receive channels (Sodickson and Manning 1997, Pruessmann *et al* 1999, Griswold *et al* 2002). Because pTx involves superposition of electromagnetic fields, there are important implications for SAR (Zhu 2004). Following the introduction of a mathematical formulation for pTx RF pulse optimization in the spatial domain (Grissom *et al* 2006), pTx has taken hold as an important tool in UHF MRI.

A parallel-transmit array coil is an essential tool in the mitigation of the B_1^+ inhomogeneity because it offers the flexibility to influence the amplitude and phase of the currents to each of the individual array elements. The experimental setup in the early work by Glover *et al* already had the capability to vary the magnitude and phase of the RF power applied to the two ports of the birdcage (Glover *et al* 1985). Ibrahim *et al* demonstrated in a numerical study the potential to achieve homogeneous B_1^+ distribution at 8T by driving the multiple ports of a 24-strut TEM volume resonator with variable phase and variable magnitude (Ibrahim *et al* 2001b). In the first multi-channel transmit array implementation by Adriany *et al* the volume resonator was split in to decoupled independent coil elements (Adriany *et al* 2005).

3.1. Definition of RF phase shimming

Figure 2(B) shows the functional block diagram of the setup used by Adriany *et al* referred to as *RF phase shimming*. Here, the amplitude of the RF pulse from each channel is equal and the phase of each channel is optimized for B_1^+ homogeneity and/or efficiency. In the figure 2(B) setup, the output power from the RFPA is split into 8 outputs of equal amplitude and phase using an 1×8 power splitter and the electrical length of the coaxial cable between the power splitter and coil input is varied to modulate the B_1^+ distribution. Eight or 16-channel versions of this setup were used in most early transmit array implementations.

3.2. Definition of static pTx

Modern UHF scanners are equipped with eight or 16 independent pTx channels, offering seamless integration of transmit arrays and providing the flexibility to vary the amplitude and phase of the currents to each of the coil elements (figure 2(C)). This version of pTx is known as static pTx or alternatively, RF/B_1^+ shimming. In static pTx the relative weights or shims are optimized between individual transmit channels. RF shimming can be performed on any RF pulse type, for example slice-selective sinc or non-selective adiabatic; the RF envelope for each channel is the same and only the RF weights vary (Padormo *et al* 2016). Although RF shimming can be broadly used in applications due to its simplicity, there are limits to the capability of static pTx to correct a heterogeous B_1^+ field, particularly as the field strength increases (Mao *et al* 2006).

3.3. Definition of dynamic pTx

A further evolution of pTx is dynamic or full-waveform pTx, where B_1^+ varies with both space and time. Here, the dynamic pTx pulse waveform is unique on each transmit channel and is typically accompanied by a set of specified excitation gradient fields. For slice-selective pTx, the most popular trajectory is the spokes trajectory (Saekho *et al* 2005, Setsompop *et al* 2006) and for non-selective pTx, it is the kT-point trajectory (Cloos *et al* 2012). Dynamic pTx leverages the full benefits of pTx by utilizing all degrees of freedom in RF pulse performance.

4. Coil configurations and transmit arrays for pTx

4.1. UHF coil configurations

Transmit arrays used in UHF imaging can be subdivided into two main categories namely TxRx arrays and ToRo arrays. In TxRx arrays, the same coil elements are used to transmit and receive, and each array element is interfaced to the scanner through a TR switch with an integrated preamplifier.

Miniaturized TR switches, assembled inside the coil housing and close to the coil elements, prevents loss in SNR due to cable losses before the preamplification stage. An 8-channel segmented loop 7T TxRx array with integrated TR switches is shown in figure 2(D) (Avdievich *et al* 2017, Paterson *et al* 2020). TxRx arrays can be closely confined to the contours of the anatomy, which provides higher transmit efficiency. However, the number of receive channels in a TxRx array is limited by the number of transmit channels, which is up to a maximum of 16 channels in state-of-the-art UHF scanners. In a recent approach aimed at increasing the number of receive channels while maintaining a tight fit, 16 additional receive-only vertical loops were combined with 16 TxRx elements. While higher SNR was measured at centre of the brain, the peripheral SNR and parallel imaging performance was lower compared to conventional receive arrays (Avdievich *et al* 2019).

Experimental multi-channel transmit system with up to 64-transmit channels have been presented (Feng et al 2012). Massively parallel TxRx coil arrays are feasible with such systems. However, tight-fitting TxRx arrays that are shaped analogous to tight-fitting receive arrays could lead to increased SAR (Avdievich *et al* 2017). Furthermore, decoupling of non-adjacent coil elements when the coil is in transmit mode could become challenging in this setup. While low impedance preamplfiers can be used to implement preamplifier decoupling (Roemer *et al* 1990) to decouple non-adjacent elements during receive mode, 50 Ω (ohm) impedance is seen by the coil elements during transmit. This requires strategies to minimize coupling between non-neighboring elements for efficient transfer of power from the RFPA to the coil

A ToRo array consists of a separate receive array in combination with a transmit array (*Barberi et al 2000*, Shajan *et al* 2014). Scanners with 64-receive channels are the current industry standard, and dedicated research scanners with up to 128 receive channels are already operational (Feinberg *et al* 2021). The ToRo configuration offers the flexibility to maximize the number of receive channels in the coil setup (Gruber *et al* 2021, Shajan *et al* 2021). Increasing the number of receive elements is essential to approach the ultimate intrinsic SNR (Ohliger *et al* 2003, Wiesinger *et al* 2004, 2005), and also take advantage of the improved parallel imaging performance offered by high density recieve arrays at UHF (Vaidya *et al* 2016).

The engineering and integration of transmit arrays with high-density receive arrays is complex and challenging. Firstly, the transmit arrays must be large enough to accommodate the receive array, which reduces transmit efficiency in addition to the attenuation of the transmit field due to the RF shielding effect caused by the receive coil elements and its electronics. This further depends on the density of receive elements in the array and its implementation. Transmit efficiency loss of 7% and 10% has been reported in 32 (*Shajan et al 2014*) and 64-channel implementations (Uğurbil *et al* 2019), respectively.

In addition, the interaction between the transmit array must be carefully controlled so that the spatial distribution of the B_1^+ field is not altered and the transmit coil performance is preserved (Shajan *et al* 2014). This can be verified by acquiring B_1^+ maps with and without the actively detuned receive array physically present within the FOV of the transmit array.

4.2. Transmit array element types

The fundamental transmit array element in most designs are based on conventional segmented loops, microstrip transmission line elements, different versions of dipole antennas or a combination of loops and dipoles. These building blocks of transmit arrays and methods to decouple them are discussed in the following sections.

4.2.1. Microstrip transmission line

The first experimental transmit array implementation was using microstrip transmission line (MTL) as array elements (Adriany *et al* 2005). Coil arrays using MTL elements were originally introduced as planar strip arrays (PSA) (Lee *et al* 2001), in which the array elements are either quarter wavelength or half wavelength long and are inherently decoupled. The individual array element consists of a narrow strip of width (w) and a ground plane separated by a low-loss dielectric substrate with thickness (h). In the original 1.5T work, w, h and the spacing between the array elements were chosen to achieve a characteristic impedance of 50 Ω, and a high dielectric substrate ($\varepsilon_r = 6.4$) was chosen to shorten the physical length because the guide wavelength (λ_g) scales by $\sqrt{\varepsilon_r}$.

In parallel, single and two turn MTL-based coil elements were proposed as alternatives to loop coils for MRI at extremely high field (Zhang *et al* 2001). The distributed nature of the transmission line allows these $\lambda/4$ structures to be suitable for high frequency applications. Furthermore, the RF shield which is part of the microstrip element reduces radiation loss, which is a prominent loss factor as the frequency of operation increases. This would result in a compact and easily implementable coils as compared to conventional loop coils which requires an additional layer for RF shielding to minimize the radiation loss at high Larmor frequencies (Ong *et al* 1995). The work by (Zhang *et al* 2001) further demonstrated that thinner substrates negatively influences the B_1^+ penetration, and substrate thickness of ⩾7 mm was required to achieve good B_1^+ penetration.

In lumped-element planar strip array (LPSA) (Lee et al 2004) implementation, the physical length of the MTL elements are shortened by terminating the ends of the microstrip with capacitors (Adriany *et al* 2005). This method allowed the physical length of the MTL elements to be dictated by the anatomy of interest and not by the wavelength as in PSA. Instead, the MTL elements are tuned to the desired frequency by adjusting the capacitors. The strip width and substrate thickness are chosen to optimize the penetration depth and the MTL elements are matched to 50 Ω through an impedance matching network. Several versions of MTL based arrays have been developed for 7T and 9.4T applications (Adriany *et al* 2010, p. 32, Vaughan *et al* 2006, Shajan *et al* 2011, Snyder *et al* 2012). The MTL elements in these early setups were tuned and matched to individual subjects before each scan session. To reduce the sensitivity of the array tuning to cable routing, the grounds of all the feed cables were shorted together at about 90 degrees from the coil input.

Center-fed MTL array (Brunner *et al* 2007) was proposed as an improved version of the $\lambda/4$ MTL array. Its symmetric feed improved the stability of the array tuning and matching, minimized the sensitivity of the array to cable routing and substantially improved the longitudinal coverage because the center-fed MTL element is essentially two $\lambda/4$ sections. A variant of the center-fed MTL element is the introduction of meanders to enhance decoupling (Orzada *et al* 2008). The size of the meanders can be further optimized to influence the decoupling and transmit performance of the array (Rietsch *et al* 2015). MTL elements with meanders is being used as the building block on the feasibility studies for scanner bore integrated massively parallel transmit array systems for body imaging at 7T (Orzada *et al* 2019, Fiedler *et al* 2021).

4.2.2. Segmented loop arrays

Loop coils have been the most widely used in MRI signal detection for more than three decades since the introduction of the NMR phased array (Ackerman *et al* 1980, Roemer *et al* 1990), but have also been used in parallel MR excitation (Setsompop *et al* 2006). The size of the individual coil element, and hence its inductance, is determined by the number of available channels, size of the overall coil, and the anatomy of interest. This is irrespective of the field strength of interest. The capacitance value needed to resonate the coil element at high Larmor frequencies can become very small and comparable to the stray capacitance between the coil and the sample. The body becomes part of the coil resonance and as a result, the coil tuning depends on the subject size and position. This capacitive coupling results in dielectric losses and exhibits as a downward shift in coil resonance, whereas inductive coupling to the sample results in an upward shift to the resonant frequency (Gadian and Robinson 1979, Ong *et al* 1995).

Multiple capacitors are evenly distributed in series, which increases the value of the individual capacitors, causing the voltage to be distributed evenly along the loop (Decorps *et al* 1985). This approach reduces the capacitive coupling, which in turn improves the robustness of the coil tuning under different loading conditions.

Optimally distributing the capacitors along the loop is a critical consideration in the design of loop coils for UHF. The number of capacitors is empirically determined by the coil designer as the trade off to consider is the increase in equivalent series resistance (ESR) due to multiple capacitors in the loop. The ratio of the unloaded coil Q-factor to the loaded coil Q-factor is a figure of merit that determines the performance of the loop (Gruber *et al* 2018). The coil input is matched to 50 Ω through a balanced matching network (Murphy-Boesch and Koretsky 1983) and a cable trap is installed close to the coil input to minimize the currents induced in the shields of the feeding cable (Peterson *et al* 2003, Seeber *et al* 2004). Cable traps also reduce parasitic coupling between coil elements and reduce sensitivity of the coil parameters to cable routing and adds stability to the S-parameter measurements. There are different types of cable traps such as the solenoid trap, the lattice balun, the sleeve or bazooka balun and the floating trap.

RF shielding is another important consideration in the design of loop coils at UHF because the radiation loss increases with frequency. A distance of 4 cm between the coil and the RF shield was found to be optimal in the study at 4T by (Ong *et al* 1995). However, UHF coils with varying distances to shields can be found in literature (Avdievich 2011, Sengupta *et al* 2016, Williams *et al* 2021a, Chu *et al* 2022). While placing the RF shield too close to the coil will negatively influence coil performance, a larger distance to the shield is sometimes not feasible especially on coils meant for scanners with head gradient inserts. Numerical simulations of UHF coils offer insights into the influence of RF shielding on coil performance. This further depends on several factors such as the operating frequency, size of the coil, anatomy of interest, sample loading as well as the scanner environment which is different for whole body and head-only gradient systems.

Neuroimaging had been the primary focus for developing UHF technology, motivated by the push to achieve high resolution functional images of the human brain. Most early loop based UHF transmit array implementations has been for imaging the human brain in 7T and 9.4T scanners (Avdievich 2011, Gilbert *et al* 2012, 2011, 2010, G. Shajan *et al* 2014, Williams *et al* 2021a) and more recently for MRI at 10.5T and 11.7T (Adriany *et al* 2019, Chu *et al* 2022). Although all of these references use segmented loops as the fundamental coil element, these examples capture a variety of implementations in terms of single and dual row coil arrangements, loose and tight-fitting coil arrays, TxRx and ToRo configurations, as well as different decoupling techniques.

4.2.3. Dipole arrays

Conventional loops and MTL elements were used as fundamental building blocks in UHF transmit arrays until dipole antenna elements were introduced (Raaijmakers *et al* 2011). The main advantage are their increased penetration depth to excite deeply located region such as the prostate which could be outside the near-field region to effectively image with surface coils. Dipole elements exhibits a nearly symmetric B_1^+ profile, whereas the conventional loop elements at UHF have a charecteristic double lobe with a strong null in between (Vaidya *et al* 2016). Radiative antenna, as it was originally named, is made of a $\lambda/2$ dipole antenna on a thick block of dielectric substrate. The high dielctric substrate was chosen to increase the directivity towards the imaging subject and its permittivity is chosen to match the average permittivity of body tissue to minimize reflections at the substrate—tissue interface.

In a concurrent work on approaching the ultimate intrinsic SNR (UISNR), the electric dipole antenna array (Wiggins *et al* 2012) was developed to mimic the ideal current patterns (Lattanzi *et al* 2010). The dipole elements were built without the thick block of dielectric subtrate. The physical length of the dipole elements was shortened by a folded end and with discrete inductors. Fractionated dipoles, introduced later (Raaijmakers *et al* 2016), are similar to the radiative antenna but without the dielectric substrate block. The optimal element length for body imaging was found to be about 30 cm, and meanders were introduced to shorten the physical length of the individual array element. The SAR efficiency of the dipole array is shown to be better than loop arrays because of the elevated SAR observed under the overlap region on loop arrays (Raaijmakers *et al* 2016). Several different versions of dipole-based coil arrays have been presented. These include the monopole antenna (Hong *et al* 2014), the folded dipole antenna (Lee *et al* 2013), the circular dipole antenna (Lakshmanan *et al* 2014), the bow-tie antenna (Oezerdem *et al* 2016), the snake antenna array (Steensma *et al* 2016) and the distributed inductance dipole antenna (Wiggins *et al* 2015), and many more.

At high frequencies for large objects, the curl-free current modes corresponding to electric dipole makes a significant contribution to UISNR at the center of the object (Lattanzi and Sodickson 2012). This was demonstrated by mixing loops and dipoles, which achieved significant improvement in central SNR at 7T (Wiggins *et al* 2013). Numerical evaluation of combined loop and dipole arrays for brain imaging at 7T also provided lower SAR compared to loop-only arrays (Eryaman *et al* 2013). Because of the distinct current distribution pattern of the loop and dipole elements, decoupling can be easily achieved by carefully aligning the two elements along their central longitudinal axis. The promise of combined use of loops and dipoles as transceivers for body imaging was demonstrated (Ertürk *et al* 2017a) as this combines the better transmit and receive performance of the loop elements at shallow depths with the superior performance of the dipoles at deeper regions.

4.3. Decoupling of transmit arrays

Decoupling of array elements is a critical consideration in the design of transmit arrays. The transmit array elements must be well-decoupled from each other to enable them to be operated independently and to be tuned and matched to 50 Ω for maximum power transfer. RF shimming to reduce B_1^+ inhomogeneity (Adriany *et al* 2005) and dynamic parallel transmission to accelerate multi-dimensional excitation (Katscher *et al* 2003, Zhu 2004) or provide efficient SAR management (Eryaman *et al* 2015, Williams *et al* 2021b) can significantly benefit from the low mutual coupling between the array elements as this enables independent control of the waveforms applied to individual transmit channels. While increasing the number of transmit elements and their arrangements provides additional degrees of flexibility to modulate the B_1^+ field, low mutual coupling between the array elements is essential to realize these benefits (Wu *et al* 2016). The performance and characteristics of coupled transmit array elements will depend on subject size and position, and results in power loss due to impedance mismatch and coupling. Furthermore, the reflected power will also depend on the excitation signal, and it becomes challenging to accurately predict coil behavior of a coupled transmit array (Kazemivalipour *et al* 2021).

Several techniques to decouple transmit array elements have been developed depending on the coil type and geometric arrangement. A rule-of-thumb in terms of S-parameters is to achieve a clear reflection response without any peak split to be able to match the individual coil elements independently to 50 Ω and to minimize power loss due to impedance mismatch and coupling The transmit architecture in the commercial systems requires each coil element to be tuned and impedance matched to transfer maximum power to a nominal load. Hence, the classic preamplifier decoupling technique (Roemer *et al* 1990) employed in receive arrays, which transforms the low input impedance of the preamplifiers to a high impedance across the coil input and creates sufficiently high isolation between the coil elements, is not feasible in transmit arrays. The transmit elements look into the 50 Ω impedance of the RF amplifier, and an analogous implementation on the transmit side requires low output impedance RF amplifiers which are not commonly available (Chu *et al* 2009).

Different experimental RF transmit amplifier architectures have been proposed recently to drive multi-channel transmit arrays (Hoult *et al* 2004, Kurpad *et al* 2006, Heilman *et al* 2007, Scott *et al* 2008, Gudino and Griswold 2013). In the on-coil current mode RF amplifier system (Gudino *et al* 2020), transmit element decoupling of less than −15 dB and high power efficiency was achieved through the high output impedance of the RF power amplifier, without any matching and decoupling circuitry.

4.3.1. Loop arrays

Geometric overlap of adjacent elements is a commonly used approach in loop-based transmit arrays (Roemer *et al* 1990). In arrays with large sized loops, the coupling between the second-neighboring elements is significant. In a recent implementation, the array loops were nested, and a pair of counter-wound inductors was used to minimize the coupling between the next-neighboring elements (Williams *et al* 2021a). In another category of loop array designs with gaps between the adjacent elements, capacitive network (Lee *et al* 2002), counter wound inductors (Kokubunji *et al* 1994), resonant inductive decoupling (RID) (Avdievich *et al* 2013), and RF shielding of the individual array elements (Gilbert *et al* 2010) have been implemented. In shared conductor design, the capacitor distribution in the common conductor between the adjacent loops is balanced to cancel the mutual coupling (Lanz *et al* 2010, Chen *et al* 2018). Self-decoupled coils, which utilize an asymmetric distribution of coil capacitance to balance and cancel the magnetic and electric coupling, has been proposed as an efficient and flexible alternative that do not impose geometric constraints (Yan *et al* 2018).

4.3.2. MTL arrays

The geometric length of PSAs (Lee *et al* 2001) is quarter or half of the resonant wavelength at the Larmor frequency. The PSA elements are inherently decoupled from each other if the element length is an integer multiple of $\lambda/4$. The LPSAs (Lee *et al* 2004) or the capacitively terminated MTLs are significantly shorter than the PSAs, and the condition for intrinsic decoupling is not achieved. The adjacent elements in an MTL array are typically achieved by interconnecting capacitors at one or both ends of the strip (Lee *et al* 2004, Adriany *et al* 2005). This is analogous to the capacitive decoupling in conventional loop coils (Lian and Roemer 1997). Moderate improvement in decoupling can be achieved by wrapping the ground plane of the microstrip element along the sidewalls of the substrate.

4.3.3. Dipole arrays

Dipole arrays when used for body imaging are tightly wrapped around the anatomy of interest and therefore the array elements are very close to the tissue. Because the antenna is heavily loaded by the tissue, the array elements are well decoupled from each other. Hence, decoupling circuits analogous to the ones used in loop array coils are not required and the array implementation becomes a straightforward arrangement of the fundamental coil elements surrounding the anatomy of interest. In situations when the dipole elements are not heavily loaded by the tissue, for example in brain imaging applications, there is strong coupling between the dipole elements which is detrimental to the transmit efficiency of the array. Passive decoupling dipoles and the RF shield have been used to improve the decoupling between the adjacent elements of the dipole array (Yan *et al* 2015, Clément *et al* 2019, Avdievich *et al* 2020, 2021).

4.4. Coil losses

The performance of a transmit array is evaluated by the B_1^+ measurement in tesla in terms of transmit efficiency for input power P, $\frac{B_1^+}{\sqrt{P}}$, and SAR efficiency or safety excitation efficiency (SEE) for simulated SAR given by $\frac{B_1^+}{\sqrt{\mathrm{SAR}}}$. Firstly, the drop in transmit efficiency at higher frequency increases the demand for high power amplifiers (Vaughan *et al* 2001). However, the output power available from the RFPA is limited. Furthermore, the cable losses between the coil input and the RFPA can be up to 3 dB and nearly half the power is wasted. Hence, engineering of transmit arrays should involve identifying and minimizing the different loss mechanisms within the coil to extract the best performance out of the transmit array.

Full-wave EM simulation tools are particularly beneficial in analyzing the efficiency metrics of the transmit array and guide the coil designer in choosing the most suitable coil configuration for the intended application. The flowchart in figure 3 captures the various loss mechanisms within the coil setup.

As shown in the flow chart, power is lost by way of reflected power due to impedance mismatch. In addition, power is lost through neighboring channels due to coupling. These losses can be minimized by achieving robust S-parameters performance in terms of excellent impedance matching and decoupling.

The cut-off frequency of the scanner bore is close to the Larmor frequency at 7T (Brunner *et al* 2009), and a significant amount of RF power applied to the transmit coil can be lost due to radiation and wave propagation (Kozlov *et al* 2018). This will result in decreased RF transmit efficiency and increased RF power absorption in the human tissue, which can significantly influence the performance of UHF transmit coils. Incorporating an RF

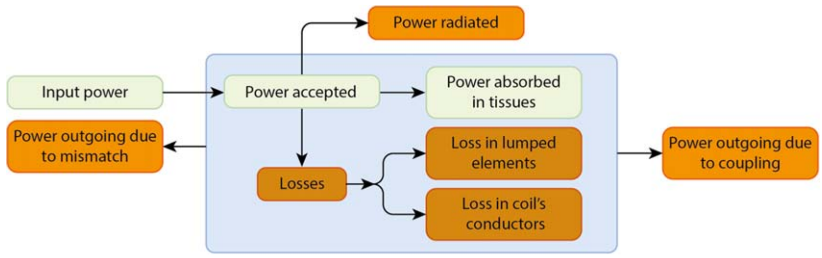

Figure 3. This flowchart captures the various loss mechanisms within a transmit array setup. The blue box represents the EM model of the coil and the body model. Transmit array designs should minimize losses due to reflection and coupling, radiation loss, and coil component losses to maximize the power delivered to the load.

shield at an appropriate distance (Avdievich 2011) from the coil elements reduces the problematic RF radiation. Furthermore, transverse electromagnetic (TEM) coil designs are inherently shielded and are widely used at UHF (Roschmann 1986, Vaughan *et al* 1994).

The RF coil losses consists of resistive losses of the coil conductors, series resistance of the components such as capacitors, inductors, diodes and radiation loss. The coil conductor losses depends on the conductivity of the material and the surface area because the RF currents flows near the surface of the conductor (Kumar *et al* 2009). The requirement for increased number of series capacitors will increase the RF circuit loss due to the ESR of the individual capacitors. It is important to select components with low ESR to minimize the series resistance as well as the potential risk of component heating due to power dissipation.

4.5. Design choice

Transmit array design for UHF MRI applications is an active field of research and it is a challenging task to provide a comprehensive comparison of different designs. A survey of UHF transmit arrays from the literature are provided in table 1. The main performance metrics of transmit array are its SAR efficiency, adequate coverage, robustness in coil performance under different loading conditions, and effective pTx performance. UHF transmit array design choice is mainly driven by the size of the anatomy. Hence, it can be broadly classified into coils for head imaging and coils for body imaging. Furthermore, head coil design principles can be easily extended to coils for extremities like knee and wrist imaging.

Conventional loop based transmit arrays have been the workhorse coils for brain imaging in 7T and 9.4T scanners. This includes both single and dual row designs. Single row designs have been shown to provide adequate whole brain coverage at 7T (e.g., 8Tx32Rx by Nova Medical Inc., MA, United States), but dual-row designs are essential to achieve whole brain excitation in 9.4T applications. 7T and 9.4T dipole based transmit arrays achieve whole brain coverage even at 9.4T with an 8-element single row design (Clément *et al* 2019, Avdievich *et al* 2021, 2022), However, it is important to note that the peak SAR_{10g} values reported at 7T are significantly higher than corresponding values reported for loop arrays (Williams *et al* 2021a), yet a direct comparison of the SAR efficiency is not currently available. Another factor to consider is the frequency shift in the tuning of dipole elements under different loading conditions (Lakshmanan *et al* 2020).

In case of body imaging, although loop-based body arrays have been developed earlier (Graessl *et al* 2013), dipole-based array elements and combinations of loops and dipoles has been the most popular choice recently due to the extended longitudinal coverage, greater penetration depth, and their ease in implementation.

Transmit array designs for extreme high field scanners such as 10.5T and 11.7T is even more challenging because of the increase in wave propagation. It has been shown recently that the coil design must be accompanied by optimization of RF shield design to maximize coil performance (Zhang *et al* 2021, Chu *et al* 2022).

5. Modelling the electromagnetic field of pTx coils

Parallel-transmit arrays in combination with pTx techniques can produce time dependent spatially varying energy deposition in biological tissue. MRI at UHF operates in a regime where quasi-static approximations are invalid and knowledge of the spatial distribution of the magnetic and electric field is essential for reliable safety assessment as well as in the management of energy deposition during an MRI examination (Collins and Smith 2001, Ibrahim and Tang 2007). Numerical simulations using heterogeneous body models are the current approach to obtain the locally varying electric and magnetic field information as well as in the estimation of tissue temperature. EM simulations have thus become an indispensable tool in demonstrating safety compliance while using pTx coils. In addition, the role of EM simulation tools is vital in the optimization of transmit arrays

Table 1. Table surveying various transmit arrays for clinical applications with suggested references.

Body region	Transmit array type	Configuration	References
Head	Loop	TxRx	Avdievich *App. Mag. Reson.* 2011; Gilbert *Mag. Reson. Med.* 2010; Gilbert *Mag. Reson. Med.* 2012; Gilbert *NMR Biomed* 2011.
		ToRo	Shajan *Mag. Reson. Med.* 2014; Williams *Front. Phys.* 2021; Uğurbil *Mag. Reson. Med.* *2019*; Uğurbil *Mag. Reson. Med.* 2019; Mareyam *Int. Soc. Mag. Reson. Med.* 2020 p0764
	Microstrip	TxRx	Adriany *Mag. Reson. Med.* 2005; Adriany *Mag. Reson. Med.* 2008; Adriany *Mag. Reson. Med.* 2010; Shajan *Mag. Reson. Med.* 2011, Orzada *Int. Soc. Mag. Reson. Med.* 2008 p2979
	Dipole	TxRx	Clément *Mag. Reson. Med.* (Vol. 81) 2019; Avdievich *NMR Biomed.* 2020; Avdievich *Mag. Reson. Med.* 2021; Connell *IEEE Trans. Med. Imag.* 2019; Tian *Int. Soc. Mag. Reson. Med.* 2016, p3524; Chen *Int. Soc. Mag. Reson. Med.* 2014 p621
		ToRo	Clément *Mag. Reson. Med.* (Vol. 82) 2019
	Loop & Dipole	TxRx	Wiggins Int. Soc. *Mag. Reson. Med.* 2013 p2737
Head & Neck	Loop	ToRo	May *Int. Soc. Mag. Reson. Med.* 2022
	Microstrip & Loop	TxRx	Pfaffenrot *Mag. Reson. Med.* *2018*
Spine	Loop	ToRo	Zhao *Mag. Reson. Med.* (Vol. 72) 2014; Zhang *Mag. Reson. Med.* (Vol. 78) 2017 Zhang *Mag. Reson. Med.* (Vol. 78) 2017
		TxRx	Kraff *Invest. Radiol.* 2009; Massire Neuroimage 2016; Vossen *J Mag. Reson.* 2011; Sigmund *NMR Biomed.* 2012; Wu *IEEE Trans. Biomed. Eng. (Vol. 57)* 2010
	Microstrip & Loop	TxRx	Rietsch *Mag. Reson. Med.* 2019
	Loop & Dipole	TxRx	Duan *Mag. Reson. Med.* 2015
Body	Dipole	TxRx	Raaijmakers *Mag. Reson. Med.* 2011; Raaijmakers *Mag. Reson. Med.* 2016; Solomakha *Mag. Reson. Med.* 2019
	Microstrip	TxRx	Fiedler *NMR Biomed.* 2021; Vaughan *Mag. Reson. Med.* 2009; Orzada *PLoS ONE* 2019
	Microstrip & Loop	ToRo	Rietsch *Med. Phys.* 2018a 2018b
	Loop & Dipole	TxRx	Paška *Mag. Reson. Med.* 2018; Ertürk *Mag. Reson. Med.* (Vol. 77 No. 1) 2017; Ertürk *Mag. Reson. Med.* (Vol. 77 No. 2); *Ertürk Topics in MRI 2019*
Cardiac	Loop	ToRo	Elabayad *Sci. Rep.* 2020
	Loop	TxRx	Gräßl *Eur. J. Radiol.* 2013
Dipole	TxRx	Oezerdem *Mag. Reson. Med.* 2016	
	Loop & Dipole	TxRx	Steensma MAGMA 2018

because it provides the necessary information to calculate the SEE (section 4.4), which is the most important performance metric of the transmit array (Avdievich *et al* 2020).

5.1. Numerical modelling of the transmit array

Electromagnetic field solvers depend upon numerical methods to solve Maxwell's equations. Early work was carried out using self-developed tools and methodologies, suited to the application and coil (Ibrahim *et al* 2000, Collins and Smith 2001).

A thorough review of the commonly available software tools used for EM simulation in MRI is beyond the scope of this paper. However, a detailed discussion can be found in (Fiedler *et al* 2018). Here we present an example using CST Studio Suite (Dassault Systèmes SE, Vélizy-Villacoublay, France) and its transient finite integration solver in conjuction with a circuit simulation co-simulaion to model the system.

The numerical model of the coil should realistically replicate the constructed coil, and the scanner environment is incorporated into the model to account for the RF wave propagation (Brunner *et al* 2009). The coil model shall consist of the mechanical model and material properties of the coil housing, the local RF shield if the transmit array is locally shielded, the RF shield in the scanner, and the coil circuits. The coil circuits consist of the input impedance matching circuit, tuning circuits, coil conductors, and decoupling circuits. To enable faster simulations by utilizing the co-simulation feature (Kozlov and Turner 2009), the tuning, matching and decoupling circuit components are defined as ports. The fixed circuit components are defined as lumped elements.

Coil component losses such as the series resistance of the capacitors, inductors, and diodes must be incorporated into the simulation environment to accurately capture the coil losses (Hoffmann *et al* 2014). Other sources of loss that could be included in the numerical model are the cable losses between the coil feedpoint and coil plug, and the insertion loss of the TR switch in the case of TxRx arrays. Further considerations include local mesh refinements to ensure all ports and lumped elements are properly connected to the coil conductors, and coarser mesh in the periphery of the simulation domain.

5.2. Example numerical model of an 8-channel transmit array

In this section we provide a 'how-to' guide to the numerical modelling using an example 8-channel TxRx array. The transmit array is a tight-fit 8-channel segmented loop TxRx array constructed on a 3 mm thick fiberglass tube with an inner cross-section of 21 cm × 24 cm (Avdievich 2011, Paterson *et al* 2020). A local RF shield is placed concentrically on an outer tube at 30 mm distance from the array elements. Adjacent array elements are decoupled by geometrical overlap, and the coil elements measure 12 cm along the *z*-direction. Custom-built TR switches with preamps are part of the coil housing. A photograph of the constructed coil array is shown in figure 2(D).

The equivalent circuit of a single array element is shown in figure 4(A). Each coil element consisted of seven fixed capacitors (C_1 to C_7; 6.8pF; C series, AT Ceramics, Huntington Station, NY, USA) and one tuning capacitor (C_8; 5610; Johanson, Camarillo, CA, USA). The input circuit consists of a balanced matching circuit with two fixed capacitors of equal value (C_9 and C_{10}) and a variable capacitor C_{11}. The loop capacitors are connected by 2 mm diameter silver plated copper wire. The coil tuning, matching, and decoupling was adjusted while loading the coil with a head and shoulder phantom filled with tissue equivalent solution (Beck *et al* 2004, Shajan *et al* 2014).

The numerical model of the 8-channel array was created in CST Studio Suite (Dassault Systèmes, Vélizy-Villacoublay, France). A screenshot of the model of a single channel is shown in figure 4(B). The matching and tuning circuits shown in schematic 4A are modelled as ports (red) and the fixed capacitors are modelled as lumped elements (blue). This enables the coil parameters to be adjusted in circuit co-simulation without the need to re-simulate in the 3D domain–effectively saving considerable simulation time (Kozlov and Turner 2009). The schematic of the input circuit included in circuit co-simulation is shown in figure 4(C). The lumped element model included ESR and equivalent series inductance (ESL) values from the component datasheet and the connecting wires are modelled as perfect electrical conductors. The coaxial cables and the cable traps are not included to minimize computational complexity. However, all losses up to the scanner coil plug consisting of the coaxial cable loss and TR switch loss are included in the model as an attenuator (figure 4(C)). This will also shift the reference power from coil input to scanner coil plug.

The numerical model also included the local shield as in the constructed coil, the two concentric fiberglass tubes ($\varepsilon = 4.3$ F m^{-1}, loss tangent = 0.025), and the scanner bore modelled as a large RF shield (Wolf *et al* 2013, Hoffmann *et al* 2014). The coil was loaded with a head-and-shoulder phantom with known electrical properties ($\varepsilon = 51.1$ F m^{-1}, $\sigma = 0.4$ S m^{-1}). A screenshot of the numerical model of the coil is shown in figure 4(D). The RF shield and fiberglass tubes are hidden for visualization.

Once a numerical model is created, the first step is to ensure that the model is robust and reliable. In this example a hexahedral mesh is used along with afinite integration solver. Although the simulation tools automatically create the mesh, it is critical to ensure that mesh has sufficient resolution for the model to avoid a staircase error. In this example the overlapping elements are sufficiently close enough that the automatic mesh may place a voxel spanning two separate coils and short them. The number of mesh cell across the lumped elements and ports may also need to be carefully considered. This is true for most of the solvers and some care and time should be assigned to improving the mesh. As such, there will be a trade-off between the ideal mesh and a practical value that is adequate, without being computationally prohibitive (Kozlov and Turner 2009). The simulation should also take care to enforce sensible boundary conditions (Fiedler *et al* 2018). Tangential electric fields should vanish at a perfectly conducting boundary and free space should be modelled using a perfectly absorbing boundary that ensures there is enough space, so that this is located outside the near field region. It is also important that the correct convergence criteria is set for an accurate solution. For example, in the transient solver the simulation will run until the energy in the system falls below a set value. In this example the convergence for the time domain solver was set to −40 dB. This criterion was set in line with the literature (Wolf

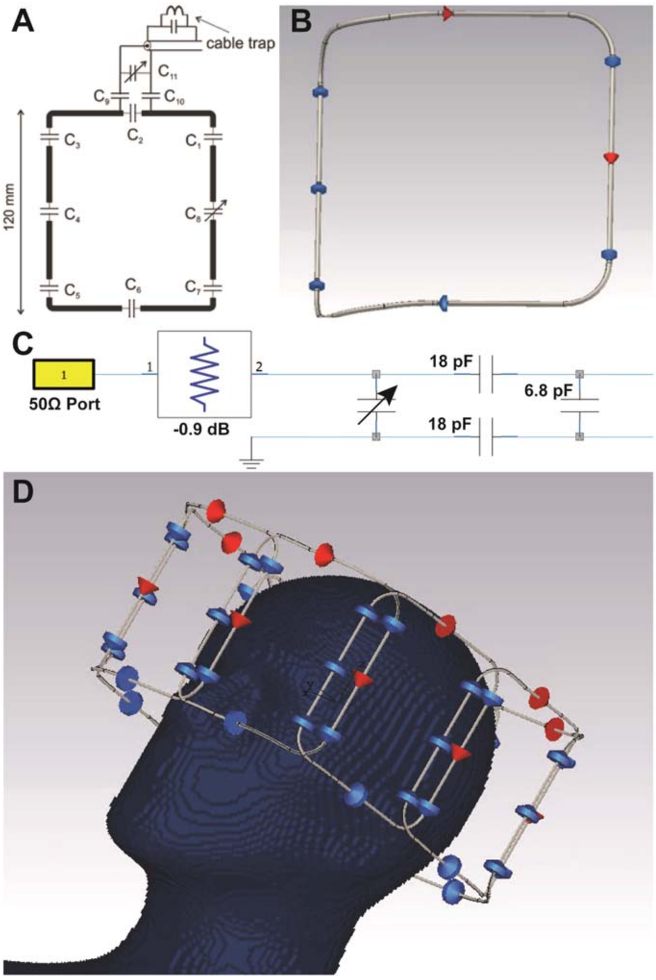

Figure 4. (A) Overview of the simulation schematic, showing the equivalent circuit for a single coil element; (B) the 3D CAD representation of this coil; (C) the schematic of the input circuit form the co- simulation in CST; (D) the 3D model of the 8Tx array, with a head-and-shoulder phantom.

et al 2013, Hoffmann *et al* 2014) as well and as a practical limit in the trade-off between simulation time and accuracy.

The next step after creating the numerical model of the transmit array is the optimization of the array S-parameters. This includes selecting suitable circuit component values to achieve S11 values of less than −30dB on each of the array elements and optimizing the overlap distance to minimize the coupling between adjacent elements. The coil tuning and matching are adjusted within a few seconds in co-simulation domain because these circuit components were modelled as ports. Optimization of the overlap distance however is adjusted iteratively and requires a new 3D simulation each time the geometry is changed until the minimum value of S21 is achieved. Figure 5(A) shows the final simulated S11 plots and adjacent element coupling (S21) for the 8-channel TxRx array, while figure 5(C) shows the same measured parameters. The highest S11 was −47 dB in simulation and −34 dB in measurement, while the worst case S21 was −15.7 dB and −18.2 dB for simulation and measurement, respectively.

Once the S-parameters are fully optimized, field maps can be generated from the fully tuned and matched system and the B_1^+ and B_1^- field maps may be derived from the simulated H-field using the following equations

$$B_1^+ = \frac{|B_{1,x} + iB_{1,y}|}{2}, \tag{4}$$

and

$$B_1^- = \frac{|B_{1,x} - iB_{1,y}|}{2}, \tag{5}$$

where $B = \mu H$, and μ is the magnetic permeability. The simulated B_1^+ maps in CP excitation mode are shown in figure 5(B) and the measured maps are shown in figure 5(D). The peak B_1^+ in simulation was 125.0 nT/V and in measurement was 108.6 nT/V. To achieve CP excitation, each coil element is driven with equal magnitude and

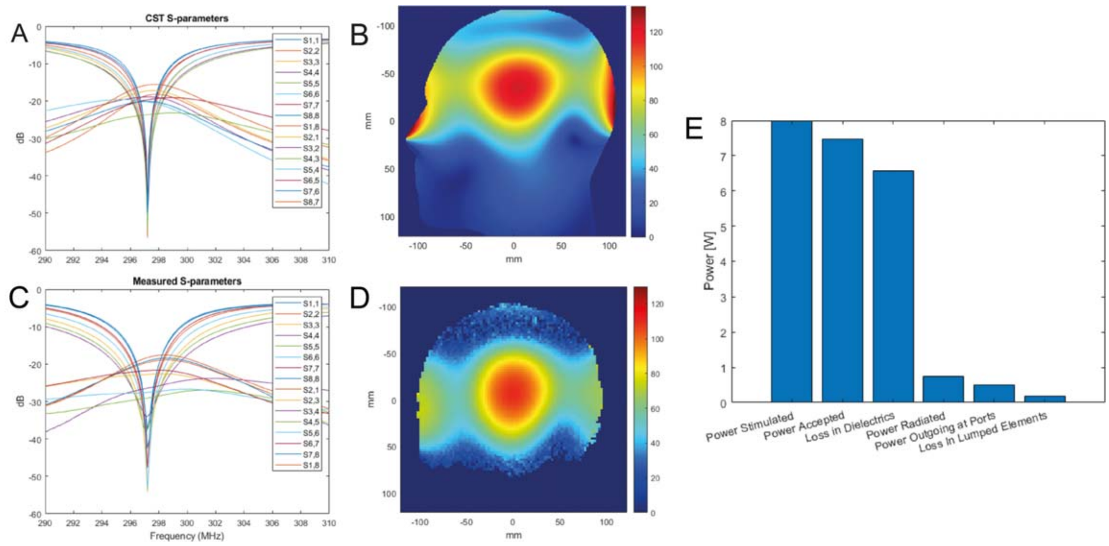

Figure 5. Example 8-channel TxRx array numerical validation. (A) Simulated and (C) measured S-parameter plots of tune and match (S11) and adjacent element coupling (S21), respectively. (B) Simulated and (D) measured B_1^+ maps in CP excitation mode. (E) The power budget, showing the distribution of the input power for the 8TxRx array.

the incremental phase offset between the adjacent channels is 45°. These values can be set as a separate excitation for the corresponding simulation ports inside the 3D solver, or if the co-simulation approach is used, they will be set here, once again providing a rapid solution for deriving the fields for an arbitrary signal.

The power budget in figure 5(E) (Kozlov and Turner 2010, Kuehne *et al* 2015) shows the distribution of the power applied to the RF coil and it captures the various losses due to the loss mechanisms outlined in section 4.4. It reveals the amount of outgoing power due to impedance mismatch and coupling (3.2%), amount of power dissipated in the coil components (1.6%), power lost due to radiation (6.6%), and the amount of power absorbed by the dielectric sample (58.1%). In addition to insights into realistic estimation of SAR per input power, the power budget provides the coil engineer with the information necessary to apply design improvements to improve the transmit efficiency of the array by minimizing the losses. This includes measures such as improving the decoupling to minimize losses due to outgoing power, RF shielding to reduce radiation loss, and selection of low loss components to minimize power dissipated in the coil components.

5.3. Validation of the numerical model

Establishing confidence in the numerical model of the coil is essential prior to SAR simulations with the coil model (Hoffmann *et al* 2014). This can be accomplished by:

(1) Comparing the values of the circuit components in the EM model with the corresponding component values in the actual coil; (2) comparing the S-parameter matrix of the simulated and constructed transmit array; (3) comparing the simulated and measured B_1^+ maps in a phantom in more than one excitation modes (for example, CP and CP^{2+} with 90° phase offsets); and (4) comparing the EM simulation-derived temperature with MR thermometry (explained in greater detail below). These simulations and measurements are performed using phantoms that load the coil comparable to the human body. The phantoms are filled with tissue equivalent solution with electrical properties of the average tissue of the anatomy of interest (Beck *et al* 2004). In the numerical domain, voxel models of the test phantoms are created and the measured electrical properties of the solution (permittivity and conductivity) are assigned for the phantom solution. For head coils, a head-and-shoulder phantom is necessary to account for loading effects of the shoulder. The entire EM simulation and validation workflow in digital phantoms up to the point of SAR simulation is shown in the first half of figure 6.

5.3.1. MR thermometry for model validation

Temperature can be both simulated and measured in specific sequences. This process, known as MR thermometry, is a critical step to validating RF coils because it corroborates the accuracy of the EM model with measured experimental data (Hoffmann *et al* 2016). The temperature rise ΔT within the model can be calculated from the EM simulated SAR (equation (2)), which is calculated from the electric fields. Given the specific heat capacity C_p of the phantom material and the pulse time Δt, we have

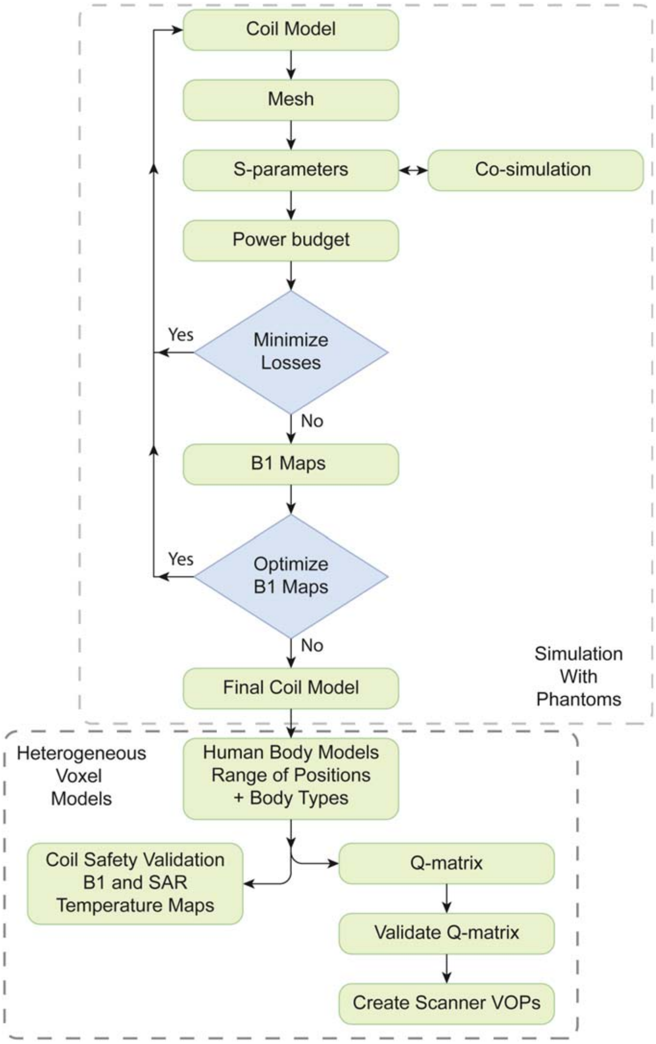

Figure 6. Workflow for performing and validating an EM field simulation of a pTx RF coil.

$$\Delta T = \frac{\mathrm{SAR} \cdot \Delta t}{C_p}. \tag{6}$$

Unlike the Pennes bioheat equation (equation (3)), this simplified version does not take diffusion and radiation into account. Nevertheless, it is a useful metric for safety evaluation when comparing the temperature rise within the scanner with the predictions on the model.

Experimentally, fluoroptic probes provide a means of measuring temperature in an MRI scanner with high precision and are a popular approach for measuring heating of implants (Mattei *et al*). However, thermal probes are only capable of measuring temperature change at point source and are furthermore invasive (Shrivastava *et al* 2011).

Instead it is desirable to map the spatially varying temperature for corroborating the EM simulation. This can be done with MRI using the proton resonance frequencey shift (PRFS) (Ishihara *et al* 1995). The PRFS method typically is performed by acquiring a series of GRE images with an additional heating pulse applied off-resonance (to avoid contaminating the imaging signal). Given a series of phase images $\Delta\varphi(\mathbf{r})$, the temperature $\Delta T(\mathbf{r})$ at location $\mathbf{r}$ is given by

$$\Delta T(\boldsymbol{r}) = \frac{\Delta\phi(\boldsymbol{r})}{\alpha\gamma B_0 TE}, \tag{7}$$

where B_0 is the main magnetic field strength, TE is the sequence echo time, γ is the gyromagnetic ratio, and α is the PRFS coefficient known to be -0.01 ppm C^{-1} in water (Ehses *et al* 2008). The PRFS method is the recommended approach for validating the EM simulation of a particular RF coil, because a matched phantom experiment can be performed to verify the accuracy of the simulation to the physical coil (Hoffmann *et al* 2016).

One disadvantage of the PRFS method is that it typically lacks high levels of precision. Given an α of -0.01 ppm C^{-1}, the sensitivity of PRFS at 7 tesla is -3Hz for 1 °C (Le Ster *et al* 2021), but magnetic field fluctuations not attributed to temperature rise are of similar orders of magnitude. This makes it challenging to reliably measure temperature changes below 1 °C even at ultra-high field strengths. Performing temperature mapping with fluoroptic probe measurements can help provide additional thermal resolution, yet remains unviable for human studies. Recently, an adapted MRI themometry approach was proposed that used the PRFS technique with improved precision by using field probes to correct for magnetic field perturbations. In conjunction with motion correction, this resulted in successful MRI thermomety performed in a set of healthy volunteers in the brain at 7T (Le Ster *et al* 2021).

5.4. Digital human body models

After the coil model is validated it can be used for SAR simulation, safety validation, and SAR management. At this point the phantom is replaced by heterogeneous human body models, which are vitally important to derive local SAR and tissue temperature distributions. Many of the simulation tools used in MRI come with a diverse range of human models from infants to geriatric, in various body types and conditions. A set of standard models from the IT'IS foundation is widely used in the community, and serve for comparisons between different coil designs (Christ *et al* 2010, Guérin *et al* 2019, Carluccio *et al* 2021, Noetscher *et al* 2021). These models are of a voxel type, which consist of a regular cuboid grid lattice with each element of the grid constituting a tissue type with corresponding material properties. It is also possible to use more complex polygonal models when using the frequency domain solvers, however, these can be quite complex to construct and may require large computational resources. Voxel models are relatively small in memory since they are represented by a simple matrix.

For reliable SAR management, a range of body models in different positions and rotations within the RF coil needs to be considered. The final SAR model can be concatenated into a single dataset (Williams *et al* 2021a). To minimize the computational burden, the body models can be truncated depending on the application. While simulating a head coil, for example, it is not necessary to include the entire anatomical body model in the simulation (Wolf *et al* 2013). This study further showed that body models that include only the head and the shoulders provides suffciently accurate results. Furthermore, the resolution in the shoulders can be modelled to be homogeneous without affecting the SAR distribution in the head, reducing the computation demands of the simulation.

5.5. SAR simulation and VOP generation

The spatially varying SAR in the case of pTx can be derived from equation (2) for time point t_i using the simulated electric field $\mathbf{E}_c$ for each N_c transmit element at all $\mathbf{r}$ voxel locations in the simulated object with known electrical conductivity and mass density (Graesslin *et al* 2012),

$$\mathrm{SAR}(\boldsymbol{r},\, t_i) = \frac{1}{\boldsymbol{V}} \int_V \frac{\sigma(\boldsymbol{r})}{2\rho(\boldsymbol{r})} \|\sum_{c=1}^{N_c} \mathrm{E}_{\boldsymbol{c}}(\boldsymbol{r},\, t_i)\|_2^2 dV. \tag{8}$$

Note here that SAR involves summing electric fields, which can lead to non-intuitve local SAR patterns. Given a normalized set of individualized $N_c \times 3$ field matrices $\tilde{\mathrm{E}}$, and a particular complex transmit vector configuration $\mathrm{w}(t_i)$,

$$\sum_{c=1}^{N_c} \mathbf{E}_{\boldsymbol{c}}(\boldsymbol{r},\, t_i) = \tilde{\mathrm{E}}(\boldsymbol{r}) \cdot \mathrm{w}(t_i)\,. \tag{9}$$

SAR can also be expressed quadractically by reformulating equation (8) in terms of so-called Q-matrices (Graesslin *et al* 2012)

$$\mathrm{SAR}(\boldsymbol{r},\, t_i) = \mathrm{w}^{\mathrm{H}}(\mathrm{t_i}) \cdot \mathbf{Q}(\boldsymbol{r}) \cdot \mathrm{w}(\mathrm{t_i}) \tag{10}$$

where

$$\mathbf{Q}(\boldsymbol{r}) = \frac{1}{\boldsymbol{V}} \int_V \frac{\sigma(\boldsymbol{r})}{2\rho(\boldsymbol{r})} \widetilde{\mathrm{E}}^{\mathrm{H}}(\boldsymbol{r}) \cdot \tilde{\mathrm{E}}(\boldsymbol{r}) dV. \tag{11}$$

The IEC safety standard for SAR is measured on averaged 10 gram volumes ('IEC 60601-2-33,' 2010). Figure 7 shows the results of SAR simulations in the example 8-channel coil model described previously.

SAR still remains the key metric to manage power deposition in MRI. For conventional sTx, the B_1^+ configuration is constant (often CP), and is conventionally monitored with a constant safety factor of SAR overestimation (so-called 'k-factor' supervision) (De Zanche *et al* 2022).

With the spatially varying SAR deposition, pTx necessitates local SAR supervision based on the simulated electromagnetic fields from a validated EM model. For any coil model simulation (or concatenated series thereof), Q-matrices (Graesslin *et al* 2012) can be formed to calculate SAR quadratically for any B_1^+ shim configuration as shown in equation (10).

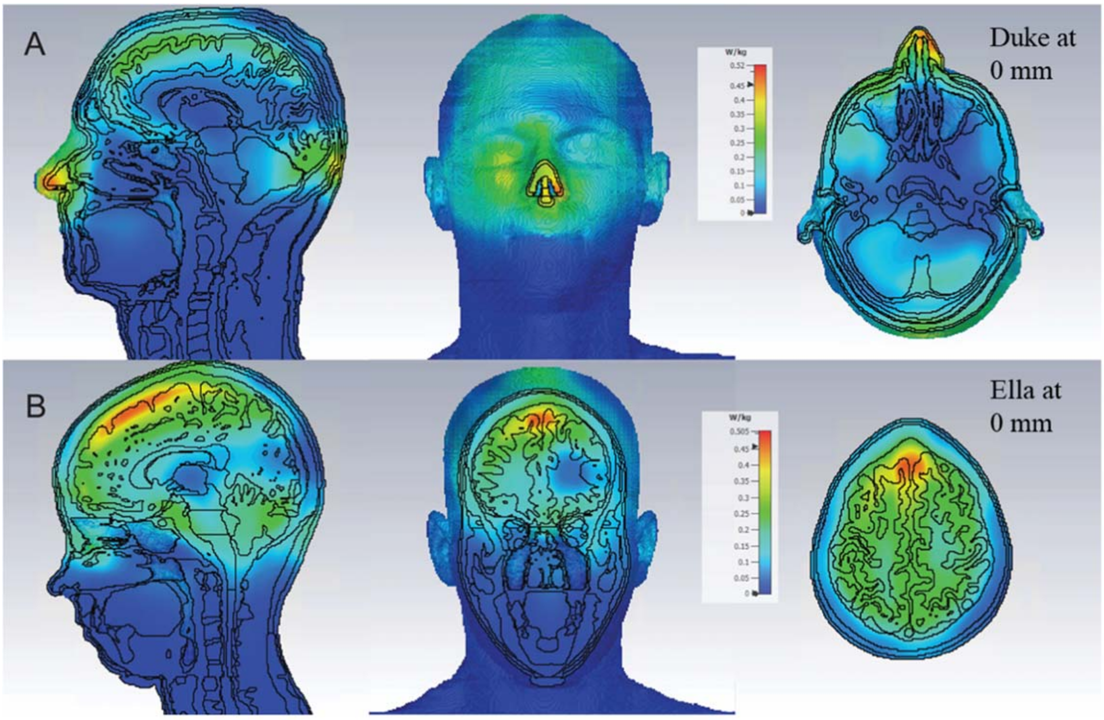

Position	Max 10 g SAR [W/kg]	Coordinates [mm]
Duke 0 mm	0.45	(10.0, 104.5, 71.5)
Duke 15 mm	0.52	(-8.5, 106.8, -72.0)
Duke 30 mm	0.52	(-4.5, 104.5, -53.5)
Ella 0 mm	0.46	(5.0, 41.5, 22.0)
Ella 15 mm	0.42	(17.0, 70.5, 61.0)
Ella 30 mm	0.51	(17.0, 70.5, 47.0)

Figure 7. SAR simulations of the (A) Duke and (B) Ella digital body models at isocenter for CP excitation given 1 W input power. Each cross-sectional slice shows the location of the peak 10 g SAR. The figure table provides maximum 10 g SAR values for 3 positions with changing z-dimension in the coil for bothbody models.

In practice, the EM simulations can result in hundreds of thousands or millions of voxels in the digital model, making online local SAR calculation computationally challenging. Virtual observation points (VOPs) offer a tractable way of estimating local SAR by exploiting the positive semidefinite properites of Q-matrices and clustering them based on their maximum eigenvalues (Eichfelder and Gebhardt 2011). The number of clusters is governed by the percent overestimation tolerated for the B_1^+ shim configuration contributing the 'worst case' or peak local SAR. A secondary work then generalizes this VOP approach to consider both upper and lower bounds of peak SAR and provides even further compression of the EM simulation (Lee *et al* 2012). Thereby, VOPs provide flexibility whereby local SAR supervision is made more or less conservative with fewer or greater numbers of VOPs, respectively. This process of SAR simulation and VOP generation in heterogeneous body models after EM model validation is shown in the latter half of figure 6.

In addition to the percent overestimation with respect to 'worst case' configuration, other safety factors can be considered in generation of VOPs for local SAR mitigation. These safety factors are outlined and described in table 2.

While conventional VOP compression outlined by Eichfelder and Gebhardt 2011 and Lee et al. 2012 remain the most popular methods for local SAR estimation in pTx, recent work has sought to improve performance. In one method using VOPs, overestimation of SAR is kept constant while the number of VOPs clusters is reduced, enabling faster pTx local SAR estimation (Orzada *et al* 2021). Another method compares overly conservative linear SAR safety factors by deriving a conditional safety factor based on probability theory (Meliadò et al 2020). Finally, a third method proposes the use of temperature VOPs in lieu of local SAR supervision to mitigate the true, relevant safety metric for pTx (Boulant et al 2016).

Table 2. Safety factors asssociated with the overestimation of local SAR using a compressed coil electromagnetic field simulation in the form of VOPs.

Safety Factor	Description and References
VOP overestimation factor	Percent overestimation for the peak local SAR, determined byVOP compression algorithm (Eichfelder and Gebhardt 2011; Lee *et al* 2012)
Scanner amplitude/phase measurement error factors	Measurement uncertainties from the directional couplers for amplitude and phase are provided by the vendor and can be incorporated into a safety factor on top of the VOPs, either through probabilistic worst case analysis (Boulant *et al* 2018) or an analytical derivation (Williams *et al* 2021a)
Intersubject variability	Incorporating multiple models at multiple positions or multiplying a single model by a constant factor (de Greef *et al* 2013; Le Garrec *et al* 2017; Ipek *et al* 2014)
Differences between measurement and simulation	Single-channel B_1^+ measurements can be calibrated and plotted against simulations. The RMSE difference can be calculated and result in an additional constant safety factor (Boulant *et al* 2018)

In general, as pTx gains popularity and widespread use, the safety considerations are of continued importance and under continuous research for improvement.

6. pTx applications and RF pulse design

To complete the discussion of pTx RF coils, it is also necessary to discuss their use. As mentioned, pTx offers additional degrees of freedom to control the transmit RF field, yet careful RF pulse design is often needed to do so. While a larger, more expansive review of pTx pulse design specifically can be found in a separate review paper (Padormo *et al* 2016), in this section we discuss pTx applications and walk through a generalized pulse design framework.

6.1. Mitigation of RF field inhomogeneity

pTx improves B_1^+ (in the case of static pTx) or flip angle homogeneity (in the case of dynamic pTx) by enabling a spatially varying RF field. Although first and most commonly explored in the human head (Ibrahim *et al* 2001b), pTx has also seen success in body (van den Bergen *et al* 2007), including the heart (Snyder *et al* 2009), the liver (Wu *et al* 2014), and the prostate (Metzger *et al* 2008).

The capacity for B_1^+ correction with pTx relies on several factors including MRI field strength, the body region being scanned, SAR, the pTx RF coil design and number of transmit elements, and the pTx RF pulse used. Given these factors, there is a theoertical upper limit to the homogenization potential of pTx (Katscher *et al* 2004).

6.2. Pulse acceleration

Although pTx is most commonly associated with mitigating flip angle inhomogeneity, pulse acceleration using the Transmit SENSE concept is another important application of pTx (Katscher *et al* 2003). Here, a shorter RF pulse length is achieved by leveraging the redundancy of pTx compared to sTx for when using RF and gradient pulses that provide spatial selection in multiple dimensions (Zhu 2004). This idea is demonstrated in figure 8, where a 2D excitation produced in single-transmit is accelerated using pTx with over a factor three improvement in excitation performance.

The use of pTx for pulse acceleration is most notable for reduced field of view (rFOV) or inner volume imaging (Feinberg *et al* 1985). For rFOV imaging, a 2D or 3D excitation pattern is generated by choosing an appropriately matched excitation gradient trajectory (e.g., spiral and EPI for 2D, stack of spirals and concentric shells for 3D) (Grissom *et al* 2006, Schneider *et al* 2013). With rFOV, the best excitation performance can be achieved when the excitation trajectory is optimized jointly with the RF waveforms (Davids *et al* 2016, Luo *et al* 2020, Majewski 2021). For the conventional sTx case, these excitation trajectories can be prohibitively long for some applications. This may lead to long RF pulse durations and thereby considerable T2 and T2* relaxation effects. For 2D rFOV imaging, pTx acceleration factors $R > 4$ have been explored while considering SAR and performance (Zelinski *et al* 2008). 2D excitation pulses have also been used *in vivo* at very high field strengths such as 9.4T (X Wu *et al* 2010). Meanwhile, the pTx tradeoff benefits of full FOV with local excitation, rFOV with $R > 6$ reduced imaging time, and rFOV with higher resolution were explored for 3D excitation have been shown (Schneider *et al* 2013).

Reduced FOV pTx pulses have since been incoporated in RARE (Hennig *et al* 1986) or turbo spin echo (TSE) sequences at 7T (Mooiweer *et al* 2018). Furthermore, the recent concept of 'Universal Pulses' (UP) derived from optimization over a database of preacquired B_1^+ and B_0 maps (Gras *et al* 2017b) has been extended to rFOV excitation, and at the UHF strength of 9.4T (Geldschläger *et al* 2021). Finally, recent work has incorporated deep learning methods into 2D rFOV excitation for single-transmit pulses (Vinding *et al* 2020) which creates the potential for such powerful artificial intelligence methods in the pTx case.

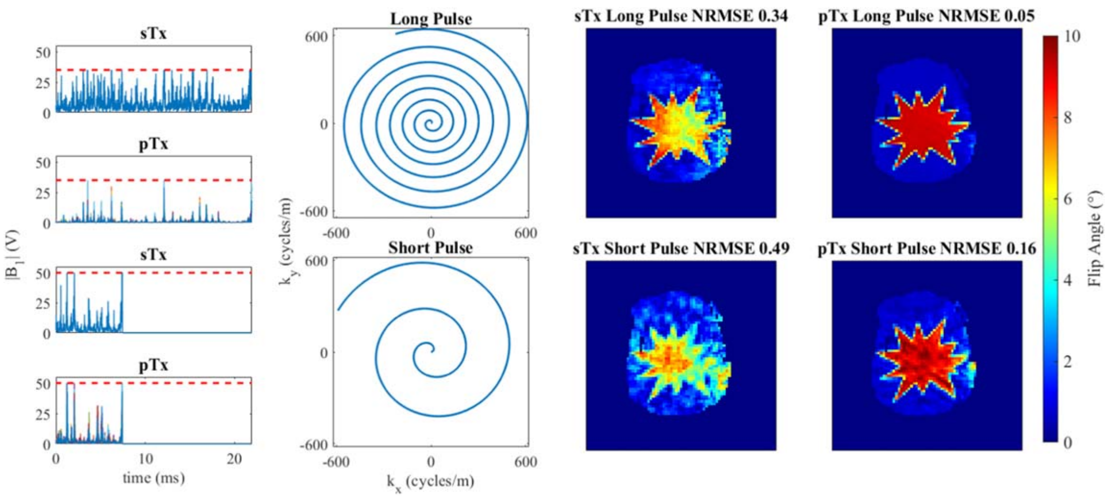

Figure 8. Toy example of using pTx for Transmit SENSE (Katscher *et al* 2003) to accelerate a 2D star excitation pattern. The left-most columns show the RF waveforms for sTx and pTx waveforms designed with two variable density spiral trajectories in the transmit k-space domain (Pauly *et al* 1989) shown in the center-left columns. Red dotted lines indicate the optimization constraint on RF voltage. Even with a prohibitively long 'Long Pulse' trajectory (~20 ms), the sTx pulse achieves poor excitation performance in terms of the normalized root mean square error (NRMSE). Meanwhile, the pTx pulse with the 'Short Pulse' trajectory achieves a low NRMSE.

6.3. Low SAR and implant-friendly RF pulses

An additional pTx application that is often less-appreciated is to alleviate SAR conditions in UHF imaging as well as in the scanning of medical device implants. pTx involves the summation of superimposed RF fields, and the local SAR distribution varies with pTx modes (Lee *et al* 2012). However, another perspective is that the additional degrees of freedom introduced with pTx offer an opportunity for better control of local SAR and associated tissue heating.

In a common pTx pulse design scenario, a pulse is optimized with specified local and global SAR constraints (Hoyos-Idrobo *et al* 2013, Guérin *et al* 2014). These constraints are especially important at higher field strengths with higher RF power deposition. Alternatively, a pTx pulse optimization can seek to minimize SAR while maintaining a standard flip angle homogeneity enforced as a constraint (Pendse *et al* 2019). More details of these pulse design formulations are discussed below in section 6.5.

Even at conventional field strengths such as 1.5 and 3 tesla, metallic implants and interventional devices pose signficiant heating risks and may be a contraindication for MRI. This can restrict a patient's healthcare, as is commonly seen in the example of patients with deep brain stimulators who could benefit greatly from MRI neuroimaging (Cabot *et al* 2013). Implant and device heating is related to the electric field and with a multi-transmit coil it is possible to generate a null mode with near-zero electric field while maintaining a desirably homogeneous B_1^+ field for imaging (Eryaman *et al* 2011, Eryaman et al 2013, Etezadi-Amoli *et al* 2015). These implant-friendly null modes have even been incorporated into pTx pulse design whereby electric field reduction and B_1^+ field homogenization are optimized simultaneously (Eryaman *et al* 2015). Recent work has sought to rigorously safety check the use of pTx for mitigating implant and device heating before use in patients and has included realistic phantom experiments (Godinez *et al* 2019, McElcheran et al 2019), *in vivo* scans in sheep (Godinez *et al* 2021), and more accurate electromagnetic field device models (Guérin *et al* 2019). This active work suggests that this strategy of pTx in patients with implants could be realized in the near future.

6.4. Tailored versus universal pulse designs

pTx RF pulses require measurement of the B_1^+ field from each individual transmit channel, which vary based on the object loaded in the coil and for each new scan occurrence. Therefore, conventional pTx RF pulse design has necessitated the measurement of subject-specific B_1^+ maps, and often static field B_0 maps as well. This appraoch to pTx pulse design is referred to as tailored pulse design and is performed online for each new subject scan.

Recently, Universal Pulses have sought to alleviate the requirement of subject-specific field map measurements (Gras *et al* 2017b). Here, a generalized pTx pulse is designed using a set of pre-acquired B_1^+ and B_0 maps from a representative population of subjects. The pulse optimization achieves robust pTx performance if performed globally over the entire test field map dataset. So far, UPs have been applied to the human head and heart (Aigner *et al* 2022). While UPs do not perform as well to their tailored counterparts, their benefit comes from eliminating scan time with additional measurements and pulse design, their ease of use (aka 'push-and-play' pTx), and their robustness to motion across the total scan session (Gras *et al* 2019).

To-date, UPs have been deployed for a variety of non-selective pulses in 3D sequences (e.g. gradient echo, MPRAGE (Mugler and Brookeman 1990), MP2RAGE (Marques *et al* 2010), FLAWS (Beaumont *et al* 2020), SPACE (Mugler 2014)) in the PASTeUR package (Massire *et al* 2022) and have been refined to overcome high B_0 field off-resonance (Van Damme *et al* 2020) using the GRAPE algorithm (Khaneja *et al* 2005). They have been extended to 2D and 3D rFOV excitations (Geldschläger *et al* 2021) and the concept has been also been used to generate calibrationaless small region shims for single-voxel spectroscopy (Berrington *et al* 2021). The recent 'Standardized Universal Pulses' have shown to achieve further robustness by employing a quick calibration scan of ~10 s (Le Ster et al 2022). Universal Pulses have been explored in a limited appraoch for slice-selection in a GRE sequence (Gras *et al* 2017a) and with simultaneous multislice (Le Ster et al 2019), yet still remains an open challenge for generalizing Universal Pulses in 2D sequences.

Another further advancement are Fast-Online Customized or FOCUS pulses (Herrler *et al* 2021a), which leverage both universal and tailored pulse designs. In the FOCUS method, a tailored pTx pulse is designed rapidly, initializing the pulse with a UP. While the FOCUS approach still requires the initial B_1^+ and B_0 map measurements for each subject, the pulse design time rapidly decreased to previous tailored approaches and also occurs fully online. Furthermore, FOCUS adapts to individual field maps that are unseen in the UP design database, which is particularly important in patient populations with irregular anatomy. FOCUS pulses were originally proposed for low flip angle 3D excitation pulses, but have since been extended to inversion pulses (Herrler *et al* 2021b) for MPRAGE. It is anticipated that FOCUS approaches can be extended to a larger class of 3D pulse sequences, similar to UPs.

6.5. How-to guide for pTx RF pulse design

Here we will describe a generalized framework for all pTx pulse design which is adaptable—from static RF shimming, to dynamic UPs; from slice-selective spokes to transmit SENSE 3D inner volume excitations. We begin with a simple formulation of an RF pulse design problem and add layers of complexity geared towards particular applications.

One of the first introduced methods of pTx RF pulse design was the spatial domain method (Grissom *et al* 2006). This approach leverages the small-tip angle (STA) approximation, which relates an RF pulse $\mathbf{b}$ and the enacted transverse magnetization $\mathbf{m}_{xy}$ through a STA system matrix, $\mathbf{A}$, that can be seen as Fourier operator incorporating B_0-induced off-resonances and a defined excitation k-space trajectory (Pauly *et al* 1989). In Grissom *et al* this is done for pTx by incorporating B_1^+ maps as diagonalized sensitivity matrices $\mathbf{S}_c$ for N_c transmit channels

$$\mathbf{m}_{xy} = \sum_{c=1}^{N_c} \mathbf{S}_c\mathbf{A}\mathbf{b}_c = \begin{bmatrix} \mathbf{S}_1\mathbf{A} & \ldots & \mathbf{S}_{N_c}\mathbf{A}\end{bmatrix}\begin{bmatrix}\mathbf{b}_1 \\ \vdots \\ \mathbf{b}_{N_c}\end{bmatrix} = \mathbf{A}_{\mathrm{pTx}}\mathbf{b}_{\mathrm{pTx}}. \tag{12}$$

Following this, an efficient way to design a pTx RF pulse is by solving a weighted, regularized least-squares problem

$$\min_{\mathbf{b}_{\mathrm{pTx}}} ||\mathbf{A}_{\mathrm{pTx}}\mathbf{b}_{\mathrm{pTx}} - \mathbf{m}_{\mathrm{T}}||_{\mathrm{W}}^2 + \lambda||\mathbf{b}_{\mathrm{pTx}}||_2^2. \tag{13}$$

Here, m_T is the target transverse magnetization, $\boldsymbol{W}$ defines the spatial weights of the design, and λ is the Tikhonov regularization parameter that penalizes the integrated RF power of the pulse, which also reduces global SAR. When the spatial domain is sufficiently small such that $\mathbf{A}_{pTx}$ is easily invertible, a closed form exists to solve for $\mathbf{b}_{\mathrm{pTx}}$, offering a simple approach for pulse design. For larger problems, iterative methods like the conjugate gradient algorithm can be used (Sutton *et al* 2003).

In the case of pTx, more advanced cost functions and optimization algorithms are often necessary. For example, consideration of local SAR and per-channel voltage limits can also be included in the cost function in the form of constraints (Hoyos-Idrobo *et al* 2013, Guérin *et al* 2014)

$$\begin{gathered}
\min_{\mathbf{b}_{\mathrm{pTx}}} ||\mathbf{A}_{\mathrm{pTx}}\mathbf{b}_{\mathrm{pTx}} - \mathbf{m}_{\mathrm{T}}||_{\mathrm{W}}^2 \\
\text{subject to} \\
\sum_{t=1}^{N_t} \mathbf{b}_{\mathrm{pTx},t}^{H}\mathbf{Q}_{\mathrm{v}}\mathbf{b}_{\mathrm{pTx},t} \leqslant \mathrm{SAR}_{\max,\,local} \quad \forall\, v = 1{:}\ N_v \\
\sum_{t=1}^{N_t} \mathbf{b}_{\mathrm{pTx},t}^{H}\mathbf{Q}_{\mathrm{G}}\mathbf{b}_{\mathrm{pTx},t} \leqslant \mathrm{SAR}_{\max,global} \\
||\mathbf{b}_{\mathrm{pTx},c}||_\infty \leqslant \mathrm{V}_{max,channel} \ \ \forall\, c = 1{:}\ N_c \\
\frac{1}{N_t}||\mathbf{b}_{\mathrm{pTx},c}||_2^2 \leqslant \mathrm{P}_{avg,\,channel} \ \ \forall\, c = 1{:}\ N_c.
\end{gathered} \tag{14}$$

The first two quadratic constraints enforce limits on local and global SAR and the second two restrict hardware voltage and average power limits, respectively. Matrices $\mathbf{Q}_v$ are a set of N_v positive semidefinite matrices representing the spatial local SAR derived from electromagnetic field simulations of the pTx coil (Graesslin *et al* 2012) while matrix $\mathbf{Q}_G$ is a single matrix to compute the global SAR. The infinity-norm (third constraint in equation (14)) limits the per-channel voltage of a pTx RF pulse, while the final 2-norm constraint limits the average per-channel power. Despite being a convex function with convex constraints, solving the cost function in equation (14) requires a solver that can handle a potentially large number of inequality constraints, but fortunately a variety of programs exist in commonly used scientific programming languages (Boyd and Vandenberghe 2004).

Despite the ease of a linear STA pulse designs, this approximation only remains valid in the STA regime, at most up to flip angles of 90° (Pauly *et al* 1989). Further works have introduced techniques to re-cast the STA approximation in terms of target flip angle (Boulant and Hoult 2012) or even by summing multiple STA designs (Grissom *et al* 2008) to acheive larger flip angles. However, to more accurately design large flip angle pTx pulses such as inversion and refocusing pulses, the nonlinear Bloch equation has been iteratively compensated for with the introduction of optimal control (Xu *et al* 2008). Optimal control methods often increase computational burden of large tip-angle (LTA) pulse design, so a popular approach is to neglect T1 and T2 relaxation and reduce the 3×3 Bloch equation rotations into the Bloch Spinor domain using Cayley-Klein parameters (Pauly *et al* 1991) or quaternions (Majewski and Ritter 2015). This generalized LTA design cost function is therefore

$$\min_{\mathbf{b}_{\mathrm{pTx}},\, \mathbf{g}_{x,y,z}} \|\mathrm{Bloch}(\mathbf{b}_{\mathrm{pTx}}, \mathbf{g}_{x,y,z}) - \mathbf{m}_{\mathrm{T}}\|_{\mathrm{W}}^2$$
$$\text{s.t. SAR and hardware constraints,} \tag{15}$$

where the STA approximation in equation (13) has been replaced by a Bloch evaluation (likely via optimal control) as a function of RF and excitation gradients. For the sake of brevity, the explicit SAR and hardware constraints in equation (14) have been summarized generically in subsequent expressions.

Excitation gradients play an important role in dynamic pTx, complementing the spatially varying RF field. Most commonly, the gradient waveforms are fixed for the pTx pulse design target. Due to design complexity, full-waveform pTx pulses don't commonly optimize every time point in a particular RF pulse, but rather at particular k-space locations. As mentioned in section 3.3, the most common trajectories for slice-selective pulses are spokes (Saekho *et al* 2005, Setsompop *et al* 2006), and for non-selective pulses are kT-points (Cloos *et al* 2012). Both spokes and kT-points are designed by optimizing the per-channel weights of RF subpulses (typically sinc for spokes, rectangular hard pulse for kT-points) and small gradient blips between subpulses. For non-selective pulses, the SPINS trajectory (Malik *et al* 2012) is also used and offers additional degrees of freedom with respect to the RF waveform optimization compared to kT-points at the expense of increased optimization complexity. Nevertheless, it is also possible to consider the joint design of RF and gradients, where the cost function in equation (15) is alternated between solving for the pTx pulse b_{pTx} and gradients $g_{x,y,z}$ to minimize the difference between Bloch-evaluated magnetization and the target. This nonlinear problem is challenging to solve, although recent approaches with auto-differntiation (Luo *et al* 2020) or explicit derivatives (Majewski 2021) offer computationally tractable solutions.

The final variation to the pTx pulse design optimization framework considered in this section is the cost function itself. Previously, equations (13)–(15) considered ordinary least-squares minimizations where a particular complex magnetization pattern is targeted. However, for many RF pulses only the magnetization magnitude or in fact the flip angle is important, so the phase can be disregarded. This leads to the formulation of a the non-convex magnitude least-squares (MLS) approach (Setsompop *et al* 2008),

$$\min_{\mathbf{b}_{\mathrm{pTx}},\, \mathbf{g}_{x,y,z}} \||\mathrm{Bloch}(\mathbf{b}_{\mathrm{pTx}}, \mathbf{g}_{x,y,z})| - \mathbf{m}_{\mathrm{T}}\|_{\mathrm{W}}^2$$
$$\text{s.t. SAR and hardware constraints,} \tag{16}$$

which can improve flip angle homogeneity compared to conventional least-squares. An MLS problem is solved by updating the target phase iteratively in a variable exchange method. Additional albeit less common cost functions have been used as well, including the minimum-SAR method from (Pendse *et al* 2019), minimum-standard deviation formulation for B_1^+ shimming (van den Bergen *et al* 2007), or even minimum-time pulse design (Aigner *et al* 2019), although it's not yet been extended to pTx.

6.6. Troubleshooting challenges with pTx pulse design

One important aspect of pTx pulse design is the challenges the pulse designer might face throughout the implementation process. In this section we mention a few common problems and offer tips on adressing them.

As discussed previously, both B_1^+ and B_0 mapping is essential for each pTx pulse design in the case of tailored RF pulses, requiring critical scan time. This compounds with the subsequenct design time associated with pulse optimization. For the case of 3D sequences, the Universal Pulse concept can help tackle the need for field mapping for an individual scan, as long as a representative population of maps exist for the initial UP creation, and also eliminates any online pulse design.

Secondly, patient motion is of concern with pTx. If using subject-specific B_1^+ and B_0 maps, these are acquired at the beginning of a scan session, and the subject can move afterwards which will reduce pulse design accuracy. This is an additional benefit of UPs, which are generally more immune to motion. Additionally, rFOV excitations are inherently less motion-sensitive. Recently, UPs have been applied to rFOV excitations (Geldschläger *et al* 2021), offering the advantages of both methods. Importantly, motion is not only detrimental to tailored pTx pulse designs, it also has potential safety implications around SAR. In the head, simulation studies of motion have found dramatic increase in SAR estimates for both RF shimming and particular dynamic pTx pulses (Ajanovic *et al* 2020, Kopanoglu *et al* 2020). Again, this is due to employing a pTx pulse designed for a set of field maps that have since changed after motion. Nevertheless, an additional solution to motion is to adapatively predict the effects of motion on B_1^+ maps using deep learning which could be used to re-design pTx pulses after motion is detected (Plumley *et al* 2021).

Alongside increasing optimization times, as pTx pulse designs become more complex with nonlinear cost functions and multiple constraints (e.g. equations (14)–(16)) they can also converge to suboptimal solutions in the form of local minima. This makes the initialization of pulse optimizations critical (Sun *et al* 2016), but recent work has rigorously studied how to enable improved solutions for non-convex pTx pulse optimizations (Eberhardt *et al* 2020). For the specific case of slice-selective spokes pulses, another recent solution using finite-difference regularization to avoid unwanted flip angle nulling has also been proposed (Paez *et al* 2021).

Finally, because pTx pulses are designed to pair with complementary excitation gradients, the fidelity of those gradients to their prescribed waveforms is crucial for pulse accuracy. This becomes increasingly more relevant with more dynamic waveforms. For fixed excitation gradients, the gradients can be measured *a priori* with calibration measurements (Duyn *et al* 1998) or Jin *et al* 2017 with additional hardware such as field probes (De Zanche *et al* 2008). When gradient waveforms are also optimized, it is still an open challenge to correct for gradient trajectory errors.

Figure 9 provides a workflow summarizing the general pTx pulse design framework, including a few considerations to make when troubleshooting.

7. Future direction for pTx

pTx RF coils and their use has been under continuous development for the past two decades and have led to significant advancements in hardware, simulation, and pulse design technology. In this final section we will discuss what lies ahead in the future for pTx including the use of artificial intelligence (AI) and the potential for routine clinical use.

7.1. Role of artificial intelligence in pTx

Machine learning and AI have recently proven to be powerful tools for various aspects of pTx. For example, AI methods have helped alleviate the computational burden of electromagnetic field simulations. In one recent work, a convolutional neural network was used to predict subject-specific local SAR given their B_1^+ maps using an 8Tx array for prostate imaging (Meliadò et al 2020). Another model generated B_1^+ maps given subject motion measurements from an initial B_1^+ maps without motion (Plumley *et al* 2021). A final recent work used generative adversarial networks to synthesize missing B_1^+ maps from a reduced subset of maps (Eberhardt et al 2022).

Artificial intelligence has also been introduced to accelerate RF pulse optimization. The 'DeepRF' deep reinforcement learning approach has been proposed to generate slice-selective excitation, slice-selective inversion, and B1-insensitive inversion pulses for single-transmit pulses (Shin *et al* 2021). Meanwhile the 'DeepControl' method uses convolutional neural networks to design 2D sTx spatial excitations for UHF (Vinding *et al* 2020). These deep learning approaches for single transmission could be extended in the future for pTx pulse design as more training data (typically B_1^+ and B_0 maps) becomes available.

Furthermore, some pTx pulse design using machine learning has already been proposed. For example in the case of static pTx, a projected ridge regression method was created to generate slice-specific shims rapidly with a subset B_1^+ mapping data (Ianni *et al* 2018). Meanwhile, the 'SmartPulse' approach offered a pTx machine learning method where a classifier learned features from the initial localizer scan to select an appropriate class of pre-designed Universal Pulses for 3T abdominal imaging (Tomi-Tricot *et al* 2019). Recently, B_1^+ map data from a 9.4T 16Tx coil was used in a regression model for spokes design in simulation (Eberhardt et al 2022).

To date, there is still some additional validation required for the role of AI in pTx in terms of accuracy and safety before these methods can be fully deployed. Nevertheless, it is clear that the computational benefits machine learning models can provide will complement the progress and development of pTx use.

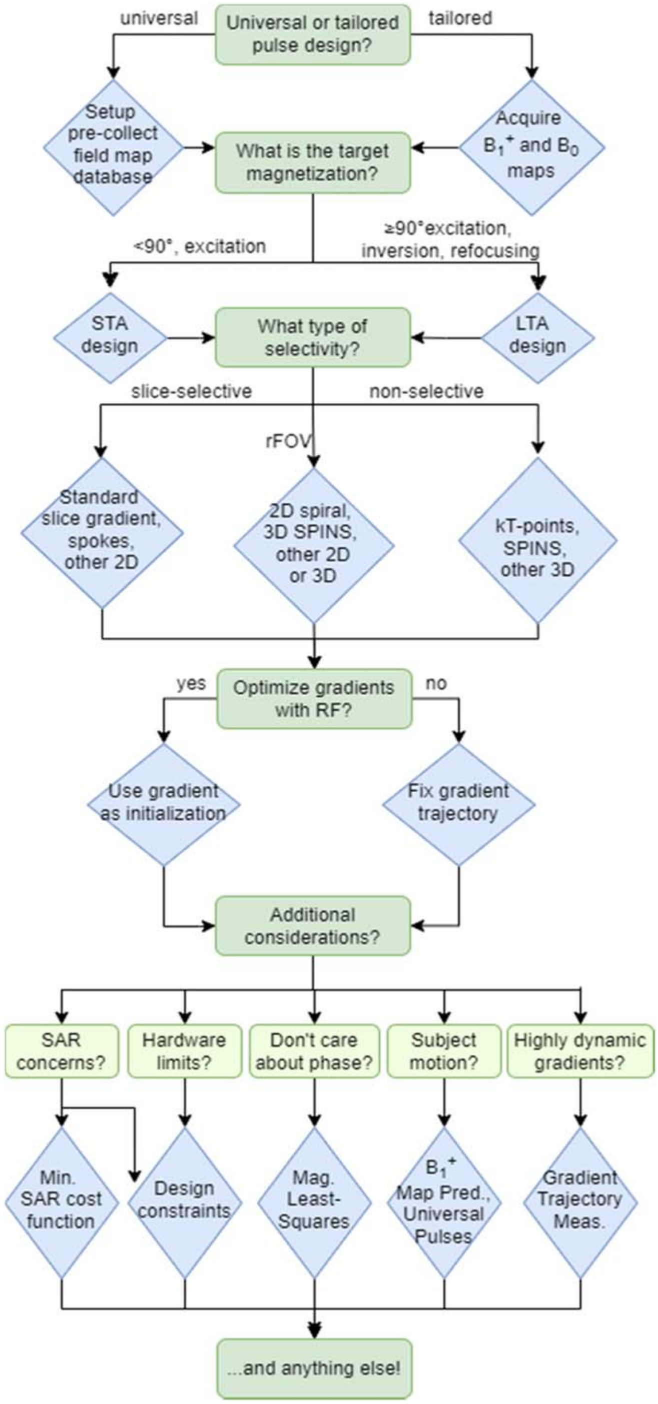

Figure 9. Workflow summarizing a general framework for pTx pulse design. The flow walks a pulse designer through a series of questions they should ask themselves and points them to relevant approaches to meet their design requirements. This outline can be extended for further pTx design complexities not considered here.

7.2. Towards regulatory approval of UHF pTx and clinical use

At the time of writing, pTx is not yet approved for regulatory use at UHF by major medical regulatory agencies such as the US Food and Drug Administration or the European Medicines Agency. This means that pTx cannot be used for diagnostic purposes, despite the advantages it offers for B_1^+ homogenization, control over SAR, and pulse acceleration.

However, modern 3 tesla scanners have two-port body coils that enable pTx using two separate transmitters. These systems are most commonly used for RF shimming for imaging in the body (Brink *et al* 2015) and also pTx applications such as rFOV imaging (Siemens' ZOOMit) (Boada *et al* 2013). These systems have improved B_1^+ homogeneity in clinical 3T imaging of large regions in the body for a variety of applications (Willinek *et al* 2010). It is expected that regulatory approval of pTx for 7T MRI could have similar or even further clinical benefits.

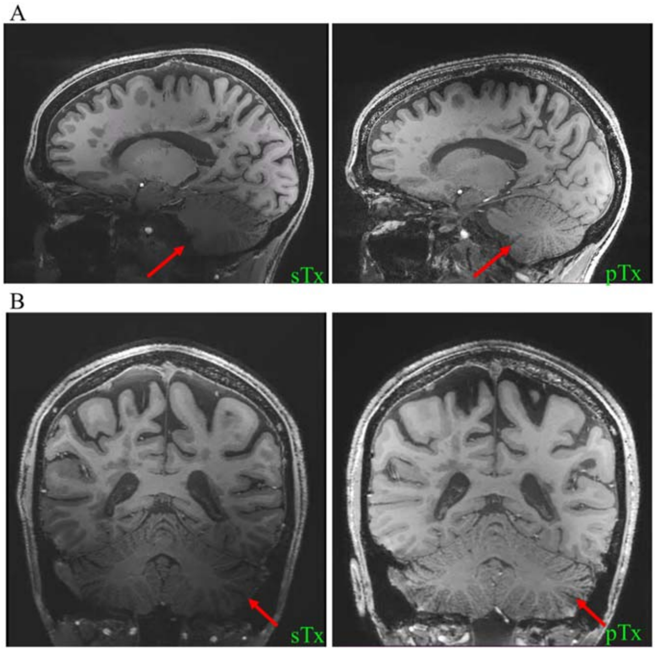

Figure 10. Example of the use of pTx MPRAGE with comparison to sTx in a clinical patient: (A) sagittal images; (B) coronal images. The pTx images show improved visualization of the cerebellum as highlighted by the red arrows. All images are windowed to have similar contrast. (Figure Credit: Jürgen Herrler, Ph.D., University Hospital Erlangen, Friedrich-Alexander-Universität Erlangen-Nürnberg (FAU), Erlangen, Germany). Reproduced with permission from Jürgen Herrler.

Currently, there are very few research publications exploring pTx in clinical populations for UHF. In the paper introducing FOCUS pulses (Herrler *et al* 2021a), an online customized pTx pulse was shown in a brain surgery patient for MPRAGE (Mugler and Brookeman 1990). Recently several works-in-progress pTx sequences have been made available on some vendor systems to support UPs through the PASTeUR package (Massire *et al* 2022) and also fully-integrated direct signal control (Malik *et al* 2015) for T2w RARE/TSE/FSE (Tomi-Tricot *et al* 2021 Thalhammer *et al* 2012). The ease of use of these research sequences have also permitted initial clinical investigations with pTx at 7T. A further example of FOCUS pTx MPRAGE in a patient with multiple sclerosis is compared to sTx MPRAGE in figure 10.

8. Conclusion

Radiofrequency coils play a key role in magnetic resonance imaging. At ultra-high field strengths, the reduced RF wavelength and increased power requirements make generating uniform excitations and thereby image homogeneity challenging. Fortunately, technological and engineering advancements in pTx RF coils can mitigate these challenges. Here we have reviewed the various transmit arrays used currently for UHF imaging and their design considerations. We have explored how to optimize coil design and to ensure safety with their generated electromagnetic fields through simulations, and have also mentioned how thermometry and local SAR monitoring contribute to the coil validation. We then explain how pTx coils are used with advanced RF pulse design and offer description of push-and-play methods such as UPs. Finally, we have provided a snapshot glimpse of the future of pTx, which is growing in use as UHF MRI becomes increasingly important for clinical imaging.

Acknowledgments

The authors would like to extend their thanks for the thoughtful commentary, suggestions, and revision help from the following colleagues: David A Porter (University of Glasgow), Sarah Allwood-Spiers (NHS Greater Glasgow & Clyde), Jürgen Herrler (FAU University Hospital Erlangen; Siemens Healthineers, Germany), Patrick Liebig (Siemens Healthineers, Germany), Belinda Ding and Iulius Dragonu (Siemens Healthineers, UK). The authors also acknowledge, UKRI Strength in Places Fund (SIPF0007/1) and UKRI Innovate UK (93468).

ORCID iDs

Sydney N Williams https://orcid.org/0000-0001-9979-6245
Paul McElhinney https://orcid.org/0000-0002-4319-0225
Shajan Gunamony https://orcid.org/0000-0002-3146-6079

References

Ackerman J J H, Grove T H, Wong G G, Gadian D G and Radda G K 1980 Mapping of metabolites in whole animals by 31P NMR using surface coils *Nature* **283** 167–70

Adriany G, Auerbach E J, Snyder C J, Gözübüyük A, Moeller S, Ritter J, Van de Moortele P-F, Vaughan T and Uğurbil K 2010 A 32-channel lattice transmission line array for parallel transmit and receive MRI at 7 tesla *Magnetic Resonance in Medicine* **63** 1478–85

Adriany G, Van de Moortele P-F, Ritter J, Moeller S, Auerbach E J, Akgün C, Snyder C J, Vaughan T and Uğurbil K 2008 A geometrically adjustable 16-channel transmit/receive transmission line array for improved RF efficiency and parallel imaging performance at 7 tesla *Magnetic Resonance in Medicine* **59** 590-597

Adriany G *et al* 2019 Evaluation of a 16-Channel Transmitter for Head Imaging at 10.5T *Int. Conf. on Electromagnetics in Advanced Applications (ICEAA) (Piscataway, NJ)* (IEEE) *(Granada, Spain)* pp 1171–4

Adriany G, Van de Moortele P-F, Wiesinger F, Moeller S, Strupp J P, Snyder C, Zhang X, Chen W, Pruessman K P, Boesinger P, Vaughan T, Uğurbil K *et al* 2005 Transmit and receive transmission line arrays for 7 Tesla parallel imaging *Magnetic Resonance in Medicine* **53** 434–45

Aigner C S, Dietrich S, Schaeffter T and Schmitter S 2022 Calibration-free pTx of the human heart at 7T via 3D universal pulses *Magnetic Resonance Medicine* **87** 70–84

Aigner C S, Rund A, Abo Seada S, Price A N, Hajnal J V, Malik S J, Kunisch K and Stollberger R 2019 Time optimal control-based RF pulse design under gradient imperfections *Magnetic Resonance in Medicine* mrm.27955 **83** 561–74

Ajanovic A, Hajnal J V and Malik S J 2020 Positional sensitivity of specific absorption rate in head at 7T *International Society for Magnetic Resonance in Medicine. (Virtual, 08/2020 pp 4251)* pp 4251

Avdievich N I 2011 Transceiver-phased arrays for human brain studies at 7 T *Applied Magnetic Resonance* **41** 483–506

Avdievich N I, Giapitzakis I A, Bause J, Shajan G, Scheffler K and Henning A 2019 Double-row 18-loop transceive–32-loop receive tight-fit array provides for whole-brain coverage, high transmit performance, and SNR improvement near the brain center at 9.4T *Magnetic Resonance in Medicine* **81** 3392–405

Avdievich N I, Hoffmann J, Shajan G, Pfrommer A, Despotović I, Scheffler K and Henning A 2017 Evaluation of transmit efficiency and SAR for a tight fit transceiver human head phased array at 9.4 T *NMR in Biomedicine* **30** 1–12

Avdievich N I, Nikulin A V, Ruhm L, Magill A W, Glang F, Henning A and Scheffler K 2022 A 32-element loop/dipole hybrid array for human head imaging at 7 T *Magnetic Resonance in Medicine* **88** 1912–26

Avdievich N I, Pan J W and Hetherington H P 2013 Resonant inductive decoupling (RID) for transceiver arrays to compensate for both reactive and resistive components of the mutual impedance *NMR in Biomedicine* **26** 1547–54

Avdievich N I, Solomakha G, Ruhm L, Henning A and Scheffler K 2021 Unshielded bent folded-end dipole 9.4 T human head transceiver array decoupled using modified passive dipoles *Magnetic Resonance in Medicine* **86** 581–97

Avdievich N I, Solomakha G, Ruhm L, Scheffler K and Henning A 2020 Decoupling of folded-end dipole atenna elements of a 9.4 T human head array using an RF shield *NMR in Biomedicine* **33** 1–11

Barberi E A, Gati J S, Rutt B K and Menon R S 2000 A transmit-only/receive-only (TORO) RF system for high-field MRI/MRS applications *Magnetic Resonance in Medicine* **43** 284–9

Barfuss H, Fischer H, Hentschel D, Ladebeck R, Oppelt A, Wittig R, Duerr W and Oppelt R 1990 *In vivo* magnetic resonance imaging and spectroscopy of humans with a 4 T whole-body magnet *NMR in Biomedicine* **3** 31–45

Barisano G, Sepehrband F, Ma S, Jann K, Cabeen R, Wang D J, Toga A W and Law M 2019 Clinical 7 T MRI: are we there yet? A review about magnetic resonance imaging at ultra-high field *BJR* **91** 1–15

Beaumont J, Gambarota G, Saint-Jalmes H, Acosta O, Ferré J-C, Raniga P and Fripp J 2020 High-resolution multi-T1–weighted contrast and T1 mapping with low B1 + sensitivity using the fluid and white matter suppression (FLAWS) sequence at 7T *Magnetic Resonance in Medicine* **85** 1364–78

Beck B L, Jenkins K A, Rocca J R and Fitzsimmons J R 2004 Tissue-equivalent phantoms for high frequencies *Concepts in Magnetic Resonance Part B: Magnetic Resonance Engineering* **20B** 30–3

Berrington A, Považan M, Mirfin C, Bawden S, Park Y W, Marsh D C, Bowtell R and Gowland P A 2021 Calibration-free regional RF shims for MRS *Magnetic Resonance in Medicine* **86** 611–624

Boada F, Shepherd T, Rosenkrantz A, Sigmund E E, Fütterer J, Chandarana H, Hagiwara M, Rusinek H, Mikheev A, Bruno M, Geppert C, Glielmi C, Pfeuffer J *et al* 2013 Parallel transmission and its clinical implementation: enabling new clinical imaging paradigms *FLASH* **7** 104–110

Bomsdorf H, Helzel T, Kunz D, Röschmann P, Tschendel O and Wieland J 1988 Spectroscopy and imaging with a 4 Tesla whole-body MR system *NMR in Biomedicine* **1** 151–8

Bottomley P A and Andrew E R 1978 RF magnetic field penetration, phase shift and power dissipation in biological tissue: implications for NMR imaging *Physics in Medicine & Biology* **23** 630–43

Boulant N and Hoult D I 2012 High tip angle approximation based on a modified bloch-riccati equation *Magnetic Resonance in Medicine* **67** 339–43

Boulant N, Wu X, Adriany G, Schmitter S, Uğurbil K and Van de Moortele P-F 2016 Direct control of the temperature rise in parallel transmission by means of temperature virtual observation points: simulations at 10.5 Tesla *Magnetic Resonance in Medicine* **75** 249–56

Boulant N, Gras V, Amadon A, Luong M, Ferrand G and Vignaud A 2018 Workflow proposal for defining SAR safety margins in parallel transmission *International Society for Magnetic Resonance in Medicine (Paris, France, 06/2018 pp 0295)*

Boyd S P and Vandenberghe L 2004 *Convex Optimization.* (Cambridge, New York: Cambridge University Press)

Brink W M, Gulani V and Webb A G 2015 Clinical applications of dual-channel transmit MRI: a review *Journal of Magnetic Resonance Imaging* **42** 855–69

Brunner D O, De Zanche N, Froehlich J, Baumann D and Pruessmann K P 2007 A symmetrically fed microstrip coil array for 7T *International Society for Magnetic Resonance in Medicine (Berlin, Germany)* p 448

Brunner D O, De Zanche N, Fröhlich J, Paska J and Pruessmann K P 2009 Travelling-wave nuclear magnetic resonance *Nature* **457** 994–8
Cabot E, Lloyd T, Christ A, Kainz W, Douglas M, Stenzel G, Wedan S and Kuster N 2013 Evaluation of the RF heating of a generic deep brain stimulator exposed in 1.5 T magnetic resonance scanners *Bioelectromagnetics* **34** 104–13
Carluccio G, Akgun C, Vaughan J T and Collins C 2021 Temperature-based MRI safety simulations with a limited number of tissues *Magnetic Resononance in Medicine* **86** 543–50
Chen G, Zhang B, Cloos M A, Sodickson D K and Wiggins G C 2018 A highly decoupled transmit–receive array design with triangular elements at 7T *Magnetic Resonance in Medicine* **80** 2267–74
Christ A, Kainz W, Hahn E G, Honegger K, Zefferer M, Neufeld E, Rascher W, Janka R, Bautz W, Chen J *et al* 2010 The virtual family—development of surface-based anatomical models of two adults and two children for dosimetric simulations *Physics in Medicine & Biology* **55** N23–38
Chu S C, Gras V, McElhinney P, Boulant N and Gundamony S 2022 Design and optimization of transmit arrays for MRI at 11.7T *International Society for Magnetic Resonance in Medicine (London, United Kingdom)* p 0706
Chu X, Yang X, Liu Y, Sabate J and Zhu Y 2009 Ultra-low output impedance RF power amplifier for parallel excitation *Magnetic Resonance in Medicine* **61** 952–61
Clément J, Gruetter R and Ipek Ö 2019 A combined 32-channel receive-Loops/8-channel transmit-dipoles coil array for whole-brain MR imaging at 7T *Magnetic Resonance in Medicine* **82** 1229–41
Clément J D, Gruetter R and Ipek Ö 2019 A human cerebral and cerebellar 8-channel transceive RF dipole coil array at 7T *Magnetic Resonance in Medicine* **81** 1447–58
Cloos M A, Boulant N, Luong M, Ferrand G, Giacomini E, Le Bihan D and Amadon A 2012 kT-points: short three-dimensional tailored RF pulses for flip-angle homogenization over an extended volume *Magnetic Resonance in Medicine* **67** 72–80
Collins C M and Smith M B 2001 Signal-to-noise ratio and absorbed power as functions of main magnetic field strength, and definition of 90° RF pulse for the head in the birdcage coil *Magnetic Resonance in Medicine* **45** 684–91
Connell I R O and Menon R S 2019 Shape optimization of an electric dipole array for 7 Tesla neuroimaging *IEEE Trans. Med. Imaging* **38** 2177–87
Davids M, Schad L R, Wald L L and Guérin B 2016 Fast three-dimensional inner volume excitations using parallel transmission and optimized K-space trajectories *Magnetic Resonance in Medicine* **76** 1170–82
Decorps M, Blondet P, Reutenauer H, Albrand J P and Remy C 1985 An inductively coupled, series-tuned NMR probe *Journal of Magnetic Resonance* **65** 100–9
de Greef M, Ipek O, Raaijmakers A J E, Crezee J and van den Berg C A T 2013 Specific absorption rate intersubject variability in 7T parallel transmit MRI of the head *Magnetic Resonance in Medicine* **69** 1476–1485
Delfino J 2014 *Criteria for Significant Risk Investigations of Magnetic Resonance Diagnostic Devices (Guidance for Industry and Food and Drug Administration Staff).* (Rockville, MD, USA: Food and Drug Administration)
Duan Q, Nair G, Gudino N, de Zwart J A, van Gelderen P, Murphy-Boesch J, Reich D S, Duyn J H and Merkle H 2015 A 7T spine array based on electric dipole transmitters *Magnetic Resonance in Medicine* **74** 1189–97
Duyn J H, Yang Y, Frank J A and van der Veen J W 1998 Simple correction method for k-space trajectory deviations in MRI *Journal of Magnetic Resonance* **132** 150–3
Eberhardt B, Poser B A, Shah N J and Felder J 2020 Application of evolution strategies to the design of SAR efficient parallel transmit multi-spoke pulses for ultra-high field MRI *IEEE Transactions on Medical Imaging* **39** 4225–36
Eberhardt B, Poser B A, Shah N J and Felder J 2022 B1 field map synthesis with generative deep learning used in the design of parallel-transmit RF pulses for ultra-high field MRI *Zeitschrift für Medizinische Physik* **32** 334–345
Ehses P, Fidler F, Nordbeck P, Pracht E D, Warmuth M, Jakob P M and Bauer W R 2008 MRI thermometry: fast mapping of RF-induced heating along conductive wires *Magnetic Resonance in Medicine* **60** 457–61
Eichfelder G and Gebhardt M 2011 Local specific absorption rate control for parallel transmission by virtual observation points *Magnetic Resonance in Medcne* **66** 1468–76
Elabyad I A, Terekhov M, Lohr D, Stefanescu M R, Baltes S and Schreiber L M 2020 A novel mono-surface antisymmetric 8Tx/16Rx coil array for parallel transmit cardiac MRI in pigs at 7T *Scientific Reports* **10** 1–183117
Ertürk M A *et al* 2017a Toward imaging the body at 10.5 Tesla *Magnetic Resonance in Medicine* **77** 434–43
Erturk M A, Li X, Van de Moortele P-F, Ugurbil K and Metzger G J 2019 Evolution of UHF body imaging in the human torso at 7T: technology, applications, and future directions *Topics MRI* **28** 101–24
Ertürk M A, Raaijmakers A J E, Adriany G, Uğurbil K and Metzger G J 2017b A 16-channel combined loop-dipole transceiver array for 7 Tesla body MRI *Magnetic Resonance in Medicine* **77** 884–94
Eryaman Y, Akin B and Atalar E 2011 Reduction of implant RF heating through modification of transmit coil electric field *Magnetic. Resonance in. Medicine.* **65** 1305–13
Eryaman Y, Guerin B, Akgun C, Herraiz J I, Martin A, Torrado-Carvajal A, Malpica N, Hernandez-Tamamos J A, Schiavi E, Adalsteinsson E, Wald L L *et al* 2015 Parallel transmit pulse design for patients with deep brain stimulation implants *Magnetic. Resonance in. Medicine.* **73** 1896–903
Eryaman Y, Turk E A, Oto C, Algin O and Atalar E 2013 Reduction of RF heating with a dual-drive birdcage coil *Magnetic. Resonance in. Medicine.* **69** 845–52
Eryaman Y, Guerin B, Kosior R, Adalsteinsson E and Wald L L 2013 Combined Loop + Dipole Arrays for 7 T brain imgaing *Int. Society for Magnetic Resonance in Medicine. ISMag. Reson. Med. (Salt Lake City, UT, USA)* p 0393
Etezadi-Amoli M, Stang P P, Kerr A B, Pauly J M and Scott G C 2015 Controlling radiofrequency-induced currents in guidewires using parallel transmit *Magnetic. Resonance in. Medicine.* **74** 1790–802
2017 FDA clears first 7T magnetic resonance imaging deviceFDA News Release fda.gov
2020 FDA Clears Most Powerful Clinical MRI Medgadget.com
Feinberg D A *et al* 2021 Design and development of a next-generation 7T human brain scanner with high-performance gradient coil and dense RF arrays *International Society for Magnetic Resonance in Medicin (Virtual pp 0562)* e.
Feinberg D A, Hoenninger J C, Crooks L E, Kaufman L, Watts J C and Arakawa M 1985 Inner volume MR imaging: technical concepts and their application *Radiology* **156** 743–7
Feng K, Hollingsworth N A, McDougall M P and Wright S M 2012 A 64-channel transmitter for investigating parallel transmit MRI *IEEE Transactions on Biomedical Engineering* **59** 2152–60
Fiedler T M, Ladd M E and Bitz A K 2018 SAR simulations & safety *NeuroImage* **168** 33–58

Fiedler T M, Orzada S, Flöser M, Rietsch S H G, Schmidt S, Stelter J K, Wittrich M, Quick H H, Bitz A K and Ladd M E 2021 Performance and safety assessment of an integrated transmit array for body imaging at 7 T under consideration of specific absorption rate, tissue temperature, and thermal dose *NMR in Biomedicine* **35** 1–17

Gadian D G and Robinson F N H 1979 Radiofrequency losses in NMR experiments on electrically conducting samples *Journal of Magnetic Resonance* **34** 449–55

Geldschläger O, Bosch D, Glaser S and Henning A 2021 Local excitation universal parallel transmit pulses at 9.4T *Magnetic Resonance in Medicine.* **86** 2589–693

Gilbert K M, Belliveau J-G, Curtis A T, Gati J S, Klassen L M and Menon R S 2012 A conformal transceive array for 7 T neuroimaging *Magnetic Resonance in Medicine* **67** 1487–96

Gilbert K M, Curtis A T, Gati J S, Martyn Klassen L, Villemaire L E and Menon R S 2010 Transmit/receive radiofrequency coil with individually shielded elements: transceive coil with individually shielded elements *Magnetic Resonance in Medicine.* **64** 1640–51

Gilbert K M, Curtis A T, Gati J S, Klassen L M and Menon R S 2011 A radiofrequency coil to facilitate B1 + shimming and parallel imaging acceleration in three dimensions at 7T *NMR in Biomedicine* **24** 815–23

Glover G H, Hayes C E, Pelc N J, Edelstein W A, Mueller O M, Hart H R, Hardy C J, O'Donnell M and Barber W D 1985 Comparison of linear and circular polarization for magnetic resonance imaging *Journal of Magnetic Resonance* **64** 255–70

Godinez F, Scott G, Padormo F, Hajnal J V and Malik S J 2019 Safe guidewire visualization using the modes of a pTx transmit array MR system *Magnetic Resonance in Medicine.* **83** 2343–2355

Godinez F, Tomi-Tricot R, Delcey M, Williams S E, Mooiweer R, Quesson B, Razavi R, Hajnal J V and Malik S J 2021 Interventional cardiac MRI using an add-on parallel transmit Mr system: *in vivo* experience in sheep *Magnetic Resonance in Medicine.* **86** 3360–72

Graessl A, Renz W, Hezel F, Dieringer M A, Winter L, Oezerdem C, Rieger J, Kellman P, Santoro D, Lindel T, Frauenrath T, Pfeiffer H, Niendor T *et al* 2013 Modular 32-channel transceiver coil array for cardiac MRI at 7.0T *Magnetic Resonance in Medicine.* **72** 276–90

Gräßl A, Winter L, Thalhammer C, Renz W, Kellman P, Martin C, von Knobelsdorff-Brenkenhoff F, Tkachenko V, Schulz-Menger J and Niendorf T 2013 Design, evaluation and application of an eight channel transmit/receive coil array for cardiac MRI at 7.0T *European . J.Journal of Radiology.* **82** 752–9

Graesslin I, Homann H, Biederer S, Börnert P, Nehrke K, Vernickel P, Mens G, Harvey P and Katscher U 2012 A specific absorption rate prediction concept for parallel transmission Mr *Magnetic Resonance in Medicine.* **68** 1664–74

Gras V, Boland M, Vignaud A, Ferrand G, Amadon A, Mauconduit F, Le Bihan D, Stöcker T and Boulant N 2017a Homogeneous non-selective and slice-selective parallel-transmit excitations at 7 Tesla with universal pulses: a validation study on two commercial RF coils *PLoS One* **12** e0183562

Gras V, Pracht E D, Mauconduit F, Le Bihan D, Stöcker T and Boulant N 2019 Robust nonadiabatic T $_2$ preparation using universal parallel-transmit k_T-point pulses for 3D FLAIR imaging at 7 T *Magnetic Resonance in Medicine* **81** 3202–8

Gras V, Vignaud A, Amadon A, Le Bihan D and Boulant N 2017 Universal Pulses: a new concept for calibration-free parallel transmission *Magnetic Resonance in Medicine* **77** 635–43

Grissom W, Yip C, Zhang Z, Stenger V A, Fessler J A and Noll D C 2006 Spatial domain method for the design of RF pulses in multicoil parallel excitation *Magnetic Resonance in Medicine* **56** 620–9

Grissom W A, Yip C-Y, Wright S M, Fessler J A and Noll D C 2008 Additive angle method for fast large-tip-angle RF pulse design in parallel excitation *Magnetic Resonance in Medicine* **59** 779–87

Griswold M A, Jakob P M, Heidemann R M, Nittka M, Jellus V, Wang J, Kiefer B and Haase A 2002 Generalized autocalibrating partially parallel acquisitions (GRAPPA) *Magnetic Resonance in Medicine* **47** 1202–10

Gruber B, Froeling M, Leiner T and Klomp D W J 2018 RF coils: a practical guide for nonphysicists: RF coils *Journal of Magnetic Resonance Imaging* **48** 590–604

Gruber B, Stockmann J P, Mareyam A, Keil B, Ghotra A, Feinberg, David A and Wald L L 2021 A 128-channel head coil array for cortical imaging at 7 Tesla *International Society for Magnetic Resonance in Medicine. Virtual* p 0176

Gudino N and Griswold M A 2013 Multi-turn transmit coil to increase B_1 efficiency in current source amplification: increased B_1 efficiency by multi-turn transmit coil *Magnetic Resonance in Medicine* **69** 1180–5

Gudino N, Zwart J A and Duyn J H 2020 Eight-channel parallel transmit-receive system for 7 T MRI with optically controlled and monitored on-coil current-mode RF amplifiers *Magnetic Resonance in Medicine* **84** 3494–501

Guérin B, Gebhardt M, Cauley S, Adalsteinsson E and Wald L L 2014 Local Specific absorption rate (SAR), global SAR, transmitter power, and excitation accuracy trade-offs in low flip-angle parallel transmit pulse design *Magnetic Resonance in Medicine* **71** 1446–57

Guérin B, Iacono M I, Davids M, Dougherty D, Angelone L M and Wald L L 2019 The 'virtual DBS population': five realistic computational models of deep brain stimulation patients for electromagnetic MR safety studies *Phys. Med. Biol.* **64** 035021

Hayes C E, Edelstein W A, Schenck J F, Mueller O M and Eash M 1985 An efficient, highly homogeneous radiofrequency coil for whole-body NMR imaging at 1.5 T *Journal of Magnetic Resonance* **63** 622–28

Hayes C E, Hattes N and Roemer P B 1991 Volume imaging with MR phased arrays *Magnetic Resonance in Medicine* **18** 309–19

Heilman J A, Riffe M J, Heid O and Griswold M A 2007 High power, high efficiency on-coil current-mode amplifier for parallel transmission arrays *International Society for Magnetic Resonance in Medicine. ISMag. Reson. Med. (Berlin, Germany)* p 171

Hennig J E, Naureth A and Friedburg H 1986 RARE imaging: a fast imaging method for clinical Mr *Magnetic Resonance in Medicine* **3** 823–33

Herrler J, Liebig P, Gumbrecht R, Ritter D, Schmitter S, Maier A, Schmidt M, Uder M, Doerfler A and Nagel A M 2021a Fast online-customized (FOCUS) parallel transmission pulses: a combination of universal pulses and individual cptimization *Magnetic Resonance in Medicine* **85** 3140–53

Herrler J, Williams S N, Liebig P, Shajan G, Meixner C, Maier A, Doerfler A, Porter D A and Nagel A M 2021b Evaluating universal and fast online customized pulses for parallel transmission using two different RF coils *International Society for Magnetic Resonance in Medicine. (Virtual)* pp 3950

Hoffmann J, Henning A, Giapitzakis I A, Scheffler K, Shajan G, Pohmann R and Avdievich N I 2016 Safety testing and operational procedures for self-developed radiofrequency coils *NMR in Biomedicine* **29** 1131–44

Hoffmann J, Shajan G, Scheffler K and Pohmann R 2014 Numerical and experimental evaluation of RF shimming in the human brain at 9.4 T using a dual-row transmit array *Magnetic Resonance Materials in Physics, Biology and Medicine* **27** 373–86

Hong S-M, Park J H, Woo M-K, Kim Y-B and Cho Z-H 2014 New design concept of monopole antenna array for UHF 7T MRI *Magnetic Resonance in Medicine* **71** 1944–52

Hoult D I 2000 Sensitivity and power deposition in a high-field imaging experiment *Journal of Magnetic Resonance Imagin* **12** 46–67

Hoult D I, Kolansky G, Kripiakevich D and King S B 2004 The NMR multi-transmit phased array: a cartesian feedback approach *Journal of Magnetic Resonance* **171** 64–70

Hoult D I and Richards R E 1976 The signal-to-noise ratio of the nuclear magnetic resonance experiment *Journal of Magnetic Resonance* **24** 71–85

Hoyos-Idrobo A, Weiss P, Massire A, Amadon A and Boulant N 2013 On variant strategies to solve the magnitude least squares optimization problem in parallel transmission pulse design and under strict SAR and power constraints *IEEE Transactions on Medical Imaging* **33** 739–48

Ianni J D, Cao Z and Grissom W A 2018 Machine learning RF shimming: prediction by iteratively projected ridge regression *Magnetic Resonance in Medicine* **80** 1871–81

Ibrahim T S 2004 A numerical analysis of radio-frequency power requirements in magnetic resonance imaging experiment *IEEE Transactions on Microwave Theory and Techniques* **52** 1999–2003

Ibrahim T S, Lee R, Abduljalil A M, Baertlein B A and Robitaille P-M L 2001a Dielectric resonances and B1 field inhomogeneity in UHF MRI: computational analysis and experimental findings *Magnetic Resonance Imaging* **19** 219–26

Ibrahim T S, Lee R, Baertlein B A, Abduljalil A M, Zhu H and Robitaille P-M L 2001b Effect of RF coil excitation on field inhomogeneity at ultra high fields: a field optimized TEM resonator *Magnetic Resonance Imaging* **19** 1339–47

Ibrahim T S, Lee R, Baertlein B A, Kangarlu A and Robitaille P-M L 2000 Application of finite difference time domain method for the design of birdcage RF head coils using multi-port excitations *Magnetic Resonance Imaging* **18** 733–42

Ibrahim T S and Tang L 2007 Insight into RF power requirements and B1 field homogeneity for human MRI via rigorous FDTD approach *Journal of Magnetic Resonance Imaging* **25** 1235–47

IEC 60601-2-33 2022 *Medical electrical equipment – Part 2-33: Particular requirements for the basic safety and essential performance of magnetic resonance equipment for medical diagnosis* International Electrotechnical Commission 306

Ipek Ö, Raaijmakers A J, Lagendijk J J, Luijten P R and van den Berg C A T 2014 Intersubject local SAR variation for 7T prostate MR imaging with an eight-channel single-side adapted dipole antenna array *Magnetic Resonance in Medicine*71 **4** 1559-1567

Ishihara Y, Calderon A, Watanabe H, Okamoto K, Suzuki Y, Kuroda K and Suzuki Y 1995 A prJinecise and fast temperature mapping using water proton chemical shift *Magnetic Resonance in Medicine* **34** 814–23

Jin J, Weber E, Destruel A, O'Brien K, Henin B, Engstrom C and Crozier S 2017 An open 8-channel parallel transmission coil for static and dynamic 7T MRI of the knee and ankle joints at multiple postures *Mag. Reson. Med.* **79** 1804–1816

Katscher U, Bornert P and van den Brink J S 2004 Theoretical and numerical aspects of transmit SENSE *IEEE Transactions on Medical Imaging* **23** 520–5

Katscher U, Börnert P, Leussler C and van den Brink J S 2003 Transmit SENSE *Magnetic Resonance in Medicine* **49** 144–50

Kazemivalipour E, Sadeghi-Tarakameh A and Atalar E 2021 Eigenmode analysis of the scattering matrix for the design of MRI transmit array coils *Mag. Reson. Med.* **85** 1727–41

Khaneja N, Reiss T, Kehlet C, Schulte-Herbrüggen T and Glaser S J 2005 Optimal control of coupled spin dynamics: design of NMR pulse sequences by gradient ascent algorithms *Journal Magnetic Resonance* **172** 296–305

Kokubunji T N, Soka T T, Kashiwa Y M, Akishima E Y and Katakura K 1994 *RF Probe for MRI.* 5,489,847 https://patents.google.com/patent/US5489847A/en 8475489

Kopanoglu E, Deniz C M, Erturk M A and Wise R G 2020 Specific absorption rate implications of within-scan patient head motion for ultra-high field MRI *Magnetic Resonance in Medicine* **84** 2724–38

Kozlov M and Turner R 2009 Fast MRI coil analysis based on 3D electromagnetic and RF circuit co-simulation *Journal of Magnetic Resonance* **200** 147–52

Kozlov M and Turner R 2010 Effects of simplifying RF coil 3D EM simulation models on power balance and SAR *International Society for Magnetic Resonance in Medicine (Stockholm, Sweden pp 1445)* p 1445

Kozlov M, Weiskopf N, Möller H E and Shajan G 2018 Reverse engineering of a 7T 16-channel dual-row transmit array coil *International Society for Magnetic Resonance in Medicine (Paris, France)* p 4412

Kraff O, Bitz A K, Kruszona S, Orzada S, Schaefer L C, Theysohn J M, Maderwald S, Ladd M E and Quick H H 2009 An eight-channel phased array RF coil for spine MR imaging at 7 T *Investigative Radiolology* **44** 734–40

Kraff O and Quick H H 2017 7T: physics, safety, and potential clinical applications: 7T: physics, safety, applications *Journal Magnetic Resonance Imaging* **46** 1573–89

Kuehne A, Goluch S, Waxmann P, Seifert F, Ittermann B, Moser E and Laistler E 2015 Power balance and loss mechanism analysis in RF transmit coil arrays: transmit array loss analysis *Magnetic Resonance in Medicine* **74** 1165–76

Kumar A, Edelstein W A and Bottomley P A 2009 Noise figure limits for circular loop MR coils *Magnetic Resonance in Medicine* **61** 1201–9

Kurpad K N, Wright S M and Boskamp E B 2006 RF current element design for independent control of current amplitude and phase in transmit phased arrays *Concepts in Magnetic Resonance Part B: Magnetic Resonance Engineering* **29B** 75–83

Lakshmanan K, Cloos M, Brown R, Lattanzi R, Sodickson D K and Wiggins G C 2020 The 'Loopole' antenna: a hybrid coil combining loop and electric dipole properties for ultra-high-field MRI *Concepts in Magnetic Resonance Part B: Magnetic Resonance Engineering* **2020** 1–9

Lakshmanan K, Cloos M A, Lattanzi R, Sodickson D K, Novikov D S and Wiggins G C 2014 The circular dipole *International Society for Magnetic Resonance in Medicine (Milan, Italy pp 0315)*

Lanz T, Müller M, Barnes H, Neubauer S and Schneider J E 2010 A high-throughput eight-channel probe head for murine MRI at 9.4 T *Magnetic Resonance in Medicine* **64** 80–7

Lattanzi R, Grant A K, Polimeni J R, Ohliger M A, Wiggins G C, Wald L L and Sodickson D K 2010 Performance evaluation of a 32-element head array with respect to the ultimate intrinsic SNR *NMR in Biomedicine* **23** 142–51

Le Garrec M, Gras V, Hang M-F, Ferrand G, Luong M and Boulant N 2017 Probabilistic analysis of the specific absorption rate intersubject variability safety factor in parallel transmission MRI *Magnetic Resonance in Medicine* **78** 1217-1223

Lattanzi R and Sodickson D K 2012 Ideal current patterns yielding optimal signal-to-noise ratio and specific absorption rate in magnetic resonance imaging: computational methods and physical insights *Magnetic Resonance in Medicine* **68** 286–304

Le Ster C, Mauconduit F, Massire A, Boulant N and Gras V 2022 Standardized universal pulse: a fast RF calibration approach to improve flip angle accuracy in parallel transmission *Magnetic Resonance in Medicine* **87** 2839–50

Le Ster C, Mauconduit F, Mirkes C, Bottlaender M, Boumezbeur F, Djemai B, Vignaud A and Boulant N 2021 RF heating measurement using MR thermometry and field monitoring: methodological considerations and first *in vivo* results *Magnetic Resonance in Medicine* **85** 1282–93

Le Ster C *et al* 2019 Comparison of SMS-EPI and 3D-EPI at 7T in an fMRI localizer study with matched spatiotemporal resolution and homogenized excitation profiles *PLoS One* **14** e0225286

Lee J, Gebhardt M, Wald L L and Adalsteinsson E 2012 Local SAR in parallel transmission pulse design *Magnetic Resonance in Medicine* **67** 1566–78

Lee R F, Giaquinto R O and Hardy C J 2002 Coupling and decoupling theory and its application to the MRI phased array *Magnetic Resonance in Medicine* **48** 203–13
Lee R F, Hardy C J, Sodickson D K and Bottomley P A 2004 Lumped-element planar strip array (LPSA) for parallel MRI *Magnetic Resonance in Medicine* **51** 172–83
Lee R F, Westgate C R, Weiss R G, Newman D C and Bottomley P A 2001 Planar strip array (PSA) for MRI *Magnetic Resonance in Medicine* **45** 673–83
Lee W, Cloos M, Sodickson D and Wiggins G 2013 Parallel transceiver array design using the modified folded dipole for 7T body applications *International Society for Magnetic Resonance in Medicine (Salt Lake City, UT, USA pp 0292)*
Lian J and Roemer P B 1997 *MRI RF Coil.* 5,804,969 https://patents.google.com/patent/US5804969A/en9695804
Luo T, Noll D C, Fessler J A and Nielsen J-F 2020 Joint design of RF and gradient waveforms via auto-differentiation for 3D tailored excitation in MRI *IEEE Transactions on Medical Imaging* **40** 3305–3314
Majewski K 2021 Simultaneous optimization of radio frequency and gradient waveforms with exact hessians and slew rate constraints applied to k T -points excitation *Journal of Magnetic Resonance* **326** 106941
Majewski K and Ritter D 2015 First and second order derivatives for optimizing parallel RF excitation waveforms *Journal of Magnetic Resonance* **258** 65–80
Malik S J, Beqiri A, Padormo F and Hajnal J V 2015 Direct signal control of the steady-state response of 3D-FSE sequences *Magnetic Resonance in Medicine* **73** 951–63
Malik S J, Keihaninejad S, Hammers A and Hajnal J V 2012 Tailored excitation in 3D with spiral nonselective (SPINS) RF pulses *Magnetic Resonance in Medicine* **67** 1303–15
Mao W, Smith M B and Collins C M 2006 Exploring the limits of RF shimming for high-field MRI of the human head *Magnetic Resonance in Medicine* **56** 918–22
Mareyam A, Kirsch J E, Chang Y, Madan G and Wald L L 2020 A 64-Channel 7T array coil for accelerated brain MRI *International Society for Magnetic Resonance in Medicine (Virtual p 0764, 08/2020)*
Marques J P, Kober T, Krueger G, van der Zwaag W, Van de Moortele P-F and Gruetter R 2010 MP2RAGE, a self bias-field corrected sequence for improved segmentation and T1-mapping at high field *NeuroImage* **49** 1271–81
Massire A, Mauconduit F, Lapert M, Naudin M, Guillevin R, Vignaud A and Boulant N 2022 PASTEUR: package of anatomical sequences using parallel transmission universal pulses now available for MAGNETOM terra *FLASH* **80** 2–13
Massire A, Taso M, Besson P, Guye M, Ranjeva J-P and Callot V 2016 High-resolution multi-parametric quantitative magnetic resonance imaging of the human cervical spinal cord at 7T *NeuroImage* **143** 58–69
Mattei E, Triventi M, Calcagnini G, Censi F, Kainz W, Bassen H I and Bartolini P 2007 Temperature and SAR measurement errors in the evaluation of metallic linear structures heating during MRI using fluoroptic® probes *Physics in Medicine & Biology* **52** 1633–46
May M W, Hansen S-L J D, Mahmutovic M, Scholz A, Kutscha N, Guerin B, Stockmann J P, Barry R L, Kazemivalipour E, Gumbrecht R, Kimmlingen R, Adriany M, Chang Y, Traintafyllou C, Knake S, Wald L L, Keil B *et al* 2022 A patient-friendly 16-channel Transmit/64-channel receive coil array for combined head–neck MRI at 7 Tesla *Mag. Reson. Med.* mrm.29288 **88** 1419–1433
McElcheran C E, Golestanirad L, Iacono M I, Wei P-S, Yang B, Anderson K J T, Bonmassar G and Graham S J 2019 Numerical simulations of realistic lead trajectories and an experimental verification support the efficacy of parallel radiofrequency transmission to reduce heating of deep brain stimulation implants during MRI *Scientific Reports* **9** 1–142124
Meliadò E F, Sbrizzi A, van den Berg C A T, Steensma B R, Luijten P R and Raaijmakers A J E 2020a Conditional safety margins for less conservative peak local SAR assessment: a probabilistic approach *Magnetic Resonance in Medicine* **84** 3379–95
Metzger G J, Snyder C, Akgun C, Vaughan T, Uğurbil K and Van de Moortele P-F 2008 Local B1 + Shimming for prostate imaging with transceiver arrays at 7T based on subject-dependent transmit phase measurements *Magnetic Resonance in Medicine* **59** 396–409 Local B1+Shimming for prostate imaging with transceiver arrays at 7T based on subject-dependent transmit phase measurements
Meliadò E F, Raaijmakers A J E, Sbrizzi A, Steensma B R, Maspero M, Savenije M H F, Luijten P R and van den Berg C A T 2020b A deep learning method for image-based subject-specific local SAR assessment *Magnetic Resonance in Medicine* **83** 695–711
Mooiweer R, Sbrizzi A, Raaijmakers A J E, van den Berg C A T, Luijten P R and Hoogduin H 2018 Phase matched RF pulse design for imaging a reduced field of excitation with a fast TSE acquisition *Magnetic Resonance Imaging* **51** 128–36
Mugler J P 2014 Optimized three-dimensional fast-spin-echo MRI *Journal of Magnetic Resonance Imaging* **39** 745–67
Mugler J P and Brookeman J R 1990 Three-dimensional magnetization-prepared rapid gradient-echo imaging (3D MP RAGE) *Magnetic Resonance in Medicine* **15** 152–7
Murphy-Boesch J and Koretsky A P 1983 An *in vivo* NMR probe circuit for improved sensitivity *Journal of Magnetic Resonance* **54** 526–32
Noetscher G M, Serano P, Wartman W A, Fujimoto K and Makarov S N 2021 Visible human project® female surface based computational phantom (nelly) for radio-frequency safety evaluation in MRI coils *PLoS ONE* **16** e0260922
Nowogrodzki A 2018 The world's strongest MRI machines are pushing human imaging to new limits *Nature*56324–6
OECD Magnetic resonance imaging (MRI) units (indicator) 09-12-2022 https://doi.org/10.1787/1a72e7d1-en
Oezerdem C, Winter L, Graessl A, Paul K, Els A, Weinberger O, Rieger J, Kuehne A, Dieringer M, Hezel F, Voit D, Frahm J, Niendorf T *et al* 2016 16-channel bow tie antenna transceiver array for cardiac MR at 7.0 Tesla *Magnetic Resonance in Medicine* **75** 2553–65
Ohliger M A, Grant A K and Sodickson D K 2003 Ultimate intrinsic signal-to-noise ratio for parallel MRI: electromagnetic field considerations *Magnetic Resonance in Medicine* **50** 1018–30
Ong K C, Wen H, Chesnick A S, Duewell S, Jaffer F A and Balaban R S 1995 Radiofrequency shielding of surface coils at 4.0T *Journal of Magnetic Resonance Imaging* **5** 773–7
Orzada S, Bahr A and Bolz T 2008 A novel 7 T microstrip element using meanders to enhance decoupling *International Society for Magnetic Resonance in Medicine (Toronto, Canada)* p 2979
Orzada S, Bitz A K, Schäfer L C, Ladd S C, Ladd M E and Maderwald S 2011 Open design eight-channel transmit/receive coil for high-resolution and real-time ankle imaging at 7 T *Medical Physics* **38** 1162–7
Orzada S, Fiedler T M, Bitz A K, Ladd M E and Quick H H 2021 Local SAR compression with overestimation control to reduce maximum relative SAR overestimation and improve multi-channel RF array performance *Magnetic Resonance Materials, Biology and Medicine* **34** 153–63
Orzada S *et al* 2019 A 32-channel parallel transmit system add-on for 7T MRI *PLoS ONE* **14** e0222452
Padormo F, Beqiri A, Hajnal J V and Malik S J 2016 Parallel transmission for ultrahigh-field imaging *NMR in Biomedicine* **29** 1145–61
Paez A, Gu C and Cao Z 2021 Robust RF shimming and small-tip-angle multispoke pulse design with finite-difference regularization *Magnetic Resonance in Medicine* **86** 1472–81
Paterson G, McElhinney P, Philliastides M G and Shajan G 2020 A tight-fit 8-channel transceiver array for simultaneous EEG-fMRI at 7-Tesla *International Society for Magnetic Resonance in Medicine (Virtual pp 4034)*

Pauly J M, Nishimura D G and Macovski A 1989 A kSpace analysis of small-tip angle excitation *Journal of Magnetic Resonance* **81** 43–56

Pauly J M, Le Roux P, Nishimura D G and Macovski A 1991 Parameter relations for the Shinnar-Le Roux selective excitation pulse design algorithm *IEEE Transactions on Medical Imaging* **10** 53–65

Paška J, Cloos M A and Wiggins G C 2018 A rigid, stand-off hybrid dipole, and birdcage coil array for 7 T body imaging *Magnetic Resonance in Medicine* **80** 822–32

Pendse M, Stara R, Mehdi Khalighi M and Rutt B 2019 IMPULSE: a scalable algorithm for design of minimum specific absorption rate parallel transmit RF pulses *Magnetic Resonance in Medicine* **81** 2808–22

Pennes H H 1948 Analysis of tissue and arterial blood temperatures in the resting human forearm *Journal of Applied Physiology* **85** 93–122

Peterson D M, Beck B L, Duensing G R and Fitzsimmons J R 2003 Common mode signal rejection methods for MRI: reduction of cable shield currents for high static magnetic field systems *Concepts in Magnetic Resonance Part B: Magnetic Resonance Engineering* **19B** 1–8

Pfaffenrot V, Brunheim S, Rietsch S H G, Koopmans P J, Ernst T M, Kraff O, Orzada S and Quick H H 2018 An 8/15-channel Tx/Rx head neck RF coil combination with region-specific B_1+ shimming for whole-brain MRI focused on the cerebellum at 7T *Magnetic Resonance in Medicine* **80** 1252–65 An 8/15-channel Tx/Rx head neck RF coil combination with region-specific B 1+shimming for whole-brain MRI focused on the cerebellum at 7T

Plumley A, Watkins L, Treder M, Liebig P, Murphy K and Kopanoglu E 2021 Rigid motion-resolved prediction using deep learning for real-time parallel-transmission pulse design *Magnetic Resonance in Medicine* **87** 2254–70

Pohmann R, Speck O and Scheffler K 2016 Signal-to-noise ratio and MR tissue parameters in human brain imaging at 3, 7, and 9.4 Tesla using current receive coil arrays: SNR at 9.4T *Magnetic Resonance in Medicine* **75** 801–9

Pruessmann K P, Weiger M, Scheidegger M B and Boesiger P 1999 SENSE: sensitivity encoding for fast MRI *Magnetic Resonance in Medicine* **42** 952–62

Raaijmakers A J E, Ipek O, Klomp D W J, Possanzini C, Harvey P, Lagendijk J J W and van den Berg C A T 2011 Design of a radiative surface coil array element at 7 T: the single-side adapted dipole antenna *Magnetic Resonance in Medicine* **66** 1488–97

Raaijmakers A J E, Luijten P R and van den Berg C A T 2016 Dipole antennas for ultrahigh-field body imaging: a comparison with loop coils *NMR in Biomedicine* **29** 1122–30

Raaijmakers A J E, Italiaander M, Voogt I J, Luijten P R, Hoogduin J M, Klomp D W J and van den Berg C A T 2016 The fractionated dipole antenna: a new antenna for body imaging at 7 Tesla *Magnetic Resonance in Medicine* **75** 1366–74

Rietsch S H G, Brunheim S, Orzada S, Voelker M N, Maderwald S, Bitz A K, Gratz M, Ladd M E and Quick H H 2019 Development and evaluation of a 16-channel receive-only RF coil to improve 7T ultra-high field body MRI with focus on the spine *Magnetic Resonance in Medicine* **82** 796–810

Rietsch S H G, Orzada S, Bitz A K, Gratz M, Ladd M E and Quick H H 2018a Parallel transmit capability of various RF transmit elements and arrays at 7T MRI *Magnetic Resonance in Medicine* **79** 1116–26

Rietsch S H G, Orzada S, Maderwald S, Brunheim S, Philips B W J, Scheenen T W J, Ladd M E and Quick H H 2018b 7T ultra-high field body MR imaging with an 8-channel transmit/32-channel receive radiofrequency coil array *Medical Physics* **45** 2978–90

Rietsch S H G, Quick H H and Orzada S 2015 Impact of different meander sizes on the RF transmit performance and coupling of microstrip line elements at 7 T: impact of different meander sizes on RF characteristics *Medical Physics* **42** 4542–52

Rinck P A 2018 *Magnetic Resonance in Medicine: A Critical Introduction* (Germany: Books on Demand GmbH) 12th edn

Robitaille P-M L, Abduljalil A M and Kangarlu A 2000 Ultra high resolution imaging of the human head at 8 Tesla: 2K × 2K for Y2K *Journal of Computer Assisted Tomography* **24** 2–8 Ultra high resolution imaging of the human head at 8 Tesla: 2K×2K for Y2K

Robitaille P-M L, Abdulijalil A M, Kangarlu A, Zhang X, Yu Y, Burgess R, Bair S, Noa P, Yang L, Zhu H, Palmer B, Jiang Z, Chakeres D M, Spigos D *et al* 1998 Human magnetic resonance imaging at 8 T *NMR in Biomedicine* **11** 263–5

Roemer P B, Edelstein W A, Hayes C E, Souza S P and Mueller O M 1990 The NMR phased array *Magnetic Resonance in Medicine* **16** 192–225

Roschmann P K H 1986 *High-frequency coil system for a magnetic resonance imaging apparatus* US4746866A

Roschmann P K H 1987 Radiofrequency penetration and absorption in the human body: limitations to high-field whole-body nuclear magnetic resonance imaging *Medical Physics* **14** 922–31

Sadeghi-Tarakameh A, Adriany G, Metzger G J, Lagore R L, Jungst S, DelaBarre L, Van de Moortele P, Uğurbil K, Atalar E and Eryaman Y 2020 Improving radiofrequency power and specific absorption rate management with bumped transmit elements in ultra-high field MRI *Magnetic Resonance in Medicine* **84** 3485–93

Saekho S, Yip C, Noll D C, Boada F E and Stenger V A 2005 Fast-kz Three-dimensional tailored radiofrequency pulse for reduced B1 inhomogeneity *Magnetic Resonance in Medicine* **55** 719–24

Schneider J T, Kalayciyan R, Haas M, Herrmann S R, Ruhm W, Hennig J and Ullmann P 2013 Inner-volume imaging *in vivo* using three-dimensional parallel spatially selective excitation *Magnetic Resonance in Medicine* **69** 1367–78

Scott G C, Stang P, Kerr A B and Pauly J M 2008 General signal vector decoupling for transmit arrays *International Society for Magnetic Resonance in Medicine (Toronto, Canada pp 1146)*

Seeber D A, Jevtic J and Menon A 2004 Floating shield current suppression trap *Concepts in Magnetic Resonance Part B: Magnetic Resonance Engineering* **21B** 26–31

Sengupta S, Roebroeck A, Kemper V G, Poser B A, Zimmermann J, Goebel R and Adriany G 2016 A specialized multi-transmit head coil for high resolution fMRI of the human visual cortex at 7T *PLoS ONE* **11** e0165418

Setsompop K, Wald L L, Alagappan V, Gagoski B, Hebrank F, Fontius U, Schmitt F and Adalsteinsson E 2006 Parallel RF transmission with eight channels at 3 Tesla *Magnetic Resonance in Medicine* **56** 1163–71

Setsompop K, Wald L L, Alagappan V, Gagoski B A and Adalsteinsson E 2008 Magnitude least squares optimization for parallel radio frequency excitation design demonstrated at 7 Tesla with eight channels *Magnetic Resonance in Medicine* **59** 908–15

Shajan G, Hoffmann J, Budde J, Adriany G, Uğurbil K and Pohmann R 2011 Design and evaluation of an RF front-end for 9.4 T human MRI *Magnetic Resonance in Medicine* **66** 594–602

Shajan G, Kozlov M, Hoffmann J, Turner R, Scheffler K and Pohmann R 2014 A 16-channel dual-row transmit array in combination with a 31-element receive array for human brain imaging at 9.4 T *Magnetic Resonance in Medicine* **71** 870–9

Shajan G, Müller R, McElhinney P, Williams S N, Groß-Weege N, Weiskopf N, Möller H E and Feinberg D 2021 A 16-channel transmit 96-channel receive head coil for NexGen 7T scanner *International Society for Magnetic Resonance in Medicine (Virtual pp 0182)*

Shin D, Kim Y, Oh C, An H, Park J, Kim J and Lee J 2021 Deep reinforcement learning-designed radiofrequency waveform in MRI *Nature Machine Intelligence* **3** 985–94

Shrivastava D, Hanson T, Kulesa J, Tian J, Adriany G and Vaughan J T 2011 Radiofrequency heating in porcine models with a 'large' 32 cm internal diameter, 7 T (296 MHz) head coil: *in vivo* RF heating at 7 T *Magnetic Resonance in Medicine* **66** 255–63

Sigmund E E, Suero G A, Hu C, McGorty K, Sodickson D K, Wiggins G C and Helpern J A 2012 High-resolution human cervical spinal cord imaging at 7 T *NMR in Biomedicine* **25** 891–9

Snyder C J, DelaBarre L, Metzger G J, van de Moortele P-F, Akgun C, Uğurbil K and Vaughan J T 2009 Initial results of cardiac imaging at 7 Tesla *Magnetic Resonance in Medicine* **61** 517–24

Snyder C J, DelaBarre L, Moeller S, Tian J, Akgun C, Van de Moortele P-F, Bolan P J, Uğurbil K, Vaughan J T and Metzger G J 2012 Comparison between eight- and sixteen-channel TEM transceive arrays for body imaging at 7 T *Magnetic Resonance in Medicine* **67** 954–64

Sodickson D K and Manning W J 1997 Simultaneous acquisition of apatial harmonics (SMASH): fast imaging with radiofrequency coil arrays *Magnetic Resonance in Medicine* **38** 591–603

Solomakha G, Leeuwen C, van, Raaijmakers A, Simovski C, Popugaev A, Abdeddaim R, Melchakova I and Glybovski S 2019 The dual-mode dipole: a new array element for 7T body imaging with reduced SAR *Magnetic Resonance Medicine* **81** 1459–69

Steensma B D, Vivian Obando Andrade A, Klomp D W J, van den Berg C A T, Luijten P R and Raaijmakers A J E 2016 Body imaging at 7 tesla with much lower SAR levels: an introduction of the snake antenna array *International Society for Magnetic Resonance in Medicine (Singapore pp 0395)*

Steensma B R, Voogt I J, Leiner T, Luijten P R, Habets J, Klomp D W J, van den Berg C A T and Raaijmakers A J E 2018 An 8-Channel Tx/Rx dipole array combined with 16 Rx loops for high-resolution functional cardiac imaging at 7 T *Magnetic Resonance Materials in Physics, Biology and Medicine* **31** 7–18

Sun H, Fessler J A, Noll D C and Nielsen J-F 2016 Joint design of excitation k-space trajectory and RF pulse for small-tip 3D tailored excitation in MRI *IEEE Transactions on Medical Imaging* **35** 468–79

Sutton B P, Noll D C and Fessler J A 2003 Fast, iterative image reconstruction for MRI in the presence of field inhomogeneities *IEEE Transactions on Medical Imaging* **22** 178–88

Thalhammer C *et al* 2012 Two-dimensional sixteen channel transmit/receive coil array for cardiac MRI at 7.0 T: design, evaluation, and application *JMRI* **36** 847–57

Tian J, Lagore R L, Delabarre L and Vaughan J T 2016 Dipole array design considerations for head MRI at 10.5T *International Society for Magnetic Resonance in Medicine (Singapore pp 3524)*

Tomi-Tricot R, Gras V, Thirion B, Mauconduit F, Boulant N, Cherkaoui H, Zerbib P, Vignaud A, Luciani A and Amadon A 2019 SmartPulse, a machine learning approach for calibration-free dynamic RF shimming: preliminary study in a clinical environment *Magnetic Resonance in Medicine* **82** 2016–31

Tomi-Tricot R, Sedlacik J, Endres J, Herrler J, Liebig P, Gumbrecht R, Ritter D, Wilkinson T, Brigden P, Giles S, Nagel A M, Hajnal J V, Neji R, Malik S J *et al* 2021 Fully integrated scanner implementation of direct signal control for 2D T2-weighted TSE at ultra-high field *International Society for Magnetic Resonance in Medicine (Virtual pp 0621)*

Uğurbil K, Auerbach E, Moeller S, Grant A, Wu X, Van de Moortele P-F, Olman C, DelaBarre L, Schillak S, Radder J, Lagore R, Adriany G *et al* 2019 Brain imaging with improved acceleration and SNR at 7 Tesla obtained with 64-channel receive array *Magnetic Resonance in Medicine* **82** 495–509

Vaidya M V, Collins C M, Sodickson D K, Brown R, Wiggins G C and Lattanzi R 2016 Dependence of B1+ and B1- field patterns of surface coils on the electrical properties of the sample and the MR operating frequency *Concepts in Magnetic Resonance Part B: Magnetic Resonance Engineering* **46** 25–40

Vaughan J T, Snyder C J, DelaBarre L J, Bolan P J, Tian J, Bolinger L, Adriany G, Andersen P, Strupp J, Ugurbil K *et al* 2009 Whole-body imaging at 7T: preliminary results*Magnetic Resonance in Medicine* **61** 244–8

Vaughan J T *et al* 2001 7T versus 4T: RF power, homogeneity, and signal-to-noise comparison in head images *Magnetic Resonance in Medicine* **46** 24–30

Vaughan J T, Hetherington H P, Otu J O, Pan J W and Pohost G M 1994 High frequency volume coils for clinical NMR imaging and spectroscopy *Magnetic Resonance in Medicine* **32** 206–18

Vaughan T, DelaBarre L, Snyder C, Tian J, Akgun C, Shrivastava D, Liu W, Olson C, Adriany G, Strupp J, Andersen P, Gopinath A, van de Moortele P-F, Garwood M, Ugurbil K *et al* 2006 9.4T human MRI: preliminary results *Magnetic Resonance in Medicine* **56** 1274–82

Van de Moortele P-F, Akgun C, Adriany G, Moeller S, Ritter J, Collins C M, Smith M B, Vaughan J T and Uğurbil K 2005 B(1) destructive interferences and spatial phase patterns at 7 T with a head transceiver array coil *Magnetic Resonance in Medicine* **54** 1503–18

Van Damme L, Mauconduit F, Chambrion T, Boulant N and Gras V 2020 Universal nonselective excitation and refocusing pulses with improved robustness to off-resonance for magnetic resonance imaging at 7 Tesla with parallel transmission *Magnetic Resonance in Medicine* **85** 678–93

van den Bergen B, van den Berg C A T, Bartels L W and Lagendijk J J W 2007 7 T body MRI: B_1 shimming with simultaneous SAR reduction *Physics in Medicine & Biology* **52** 5429–41

Vinding M S, Aigner C S, Schmitter S and Lund T E 2020 DeepControl: 2D RF pulses facilitating B1 + inhomogeneity and B0 off-resonance compensation *in vivo* at 7T *Magnetic Resonance in Medicine* **85** 3308–17

Vossen M, Teeuwisse W, Reijnierse M, Collins C M, Smith N B and Webb A G 2011 A Radiofrequency coil configuration for imaging the human vertebral column at 7T *Journal of Magnetic Resonance* **208** 291–7

Webb A G and Collins C M 2010 Parallel transmit and receive technology in high-field magnetic resonance neuroimaging *International Journal of Imaging Systems and Technology* **20** 2–13

Wiesinger F, Boesiger P and Pruessmann K P 2004 Electrodynamics and ultimate SNR in parallel MR imaging *Magnetic Resonance in Medicine* **52** 376–90

Wiesinger F, De Zanche N and Pruessmann K P 2005 Approaching ultimate SNR with finite coil arrays *International Society for Magnetic Resonance in Medicine (Miami Beach, FL, USA pp 672)*

Wiggins C J, Hang M-F, Amadon A, Cloos M, Boulant N, Luong M, Ferrand G and Edler K 2012 Combining cylindrically mounted dipoles with loops on a transverse plane for better head coverage in parallel transmission *International Society for Magnetic Resonance in Medicine (Melbourne, Australia pp 2783)*

Wiggins C J, Zhang B, Cloos M A, Lattanzi R, Chen G, Lakshmanan K, Haemer G G and Sodickson D K 2013 Mixing loops and electric dipole antennas for increased sensitivity at 7 Tesla *International Society for Magnetic Resonance in Medicine (Salt Lake City, UT, USA pp 2737)*

Wiggins G C, Lakshmanan K and Chen G 2015 The distributed inductance electric dipole antenna *International Society for Magnetic Resonance in Medicine (Toronto, Canada pp 3100)*

Williams S N, Allwood-Spiers S, McElhinney P, Paterson G, Herrler J, Liebig P, Nagel A M, Foster J E, Porter D A and Gunamony S 2021a A nested eight-channel transmit array with open-face concept for human brain imaging at 7 Tesla *Frontiers in Physics* **9** 1–16701330

Williams S N, Herrler J, Liebig P, McElhinney P, Shajan G, Nagel A M and Porter D A 2021b SAR management in pTx sequence design: the impact of electromagnetic-field-derived virtual observation points *International Society for Magnetic Resonance in Medicine (Virtual pp 0412)* p 0412

Willinek W A, Gieseke J, Kukuk G M, Nelles M, König R, Morakkabati-Spitz N, Träber F, Thomas D, Kuhl C K and Schild H H 2010 Dual-source parallel radiofrequency excitation body MR imaging compared with standard MR imaging at 3.0 T: initial clinical experience *Radiology* **256** 966–75

Wolf S, Diehl D, Gebhardt M, Mallow J and Speck O 2013 SAR simulations for high-field MRI: how much detail, effort, and accuracy is needed? *Magnetic Resonance in Medicine* **69** 1157–68

Wu B, Chunsheng W, Kelley D A C, Duan X, Vigneron D B, Nelson S J and Zhang X 2010 Shielded microstrip array for 7T human MR imaging *IEEE Transactions on Medical Imaging* **29** 179–84

Wu B, Wang C, Bammer R, Kelley D A, Xu Duan, Pang Yong, Banerjee S, Vigneron D B, Nelson S J, Majumdar S and Zhang X 2010 7T human spine imaging arrays with adjustable inductive decoupling *IEEE Transactions on Biomedical Engineering* **57** 397-403

Wu X, Schmitter S, Auerbach E J, Ugurbil K and Van de Moortele PF 2014 Mitigating transmit B1 inhomogeneity in the liver at 7T using multi-spoke parallel transmit RF pulse design *Quantitative Imaging in Medicine and Surgery* **4** 4–10

Wu X, Tian J, Schmitter S, Vaughan J T, Uğurbil K and Van de Moortele P-F 2016 Distributing coil elements in three dimensions enhances parallel transmission multiband RF performance: a simulation study in the human brain at 7 Tesla *Magnetic Resonance in Medicine* **75** 2464–72

Wu X, Vaughan J T, Uğurbil K and Van de Moortele P-F 2010 Parallel excitation in the human brain at 9.4 T counteracting *k* -space errors with RF pulse design *Magnetic Resonance in Medicine* **63** 524–9

Xu D, King K F, Zhu Y, McKinnon G C and Liang Z-P 2008 Designing multichannel, multidimensional, arbitrary flip angle RF pulses using an optimal control approach *Magnetic Resonance in Medicine* **59** 547–60

Yan X, Gore J C and Grissom W A 2018 Self-decoupled radiofrequency coils for magnetic resonance imaging *Nature Communications* **9** 1–12 3481

Yan X, Wei L, Xue R and Zhang X 2015 Hybrid monopole/loop coil array for human head MR imaging at 7 T *Applied Magnetic Resonance* **46** 541–50

Yang Q X, Wang J, Zhang X, Collins C M, Smith M B, Liu H, Zhu X-H, Vaughan J T, Uğurbil K and Chen W 2002 Analysis of wave behavior in lossy dielectric samples at high field *Magnetic Resonance in Medicine* **47** 982–9

De Zanche N *et al* 2022 *ISMRM best practices for safety testing of experimental RF hardware* International Society for Magnetic Resonance in Medicine 1–119 https://www.ismrm.org/safety/RF_Hardware_Safety_Testing_2022-03.pdf

De Zanche N, Barmet C, Nordmeyer-Massner J A and Pruessmann K P 2008 NMR probes for measuring magnetic fields and field dynamics in MR systems *Magnetic Resonance in Medicine* **60** 176–86

Zelinski A C, Angelone L M, Goyal V K, Bonmassar G, Adalsteinsson E and Wald L L 2008 Specific absorption rate studies of the parallel transmission of inner-volume excitations at 7T *Journal of Magnetic Resonance Imaging* **28** 1005–18

Zhang B, Adriany G, Delabarre L, Radder J, Lagore R, Rutt B, Yang Q X, Uğurbil K and Lattanzi R 2021 Effect of radiofrequency shield diameter on signal-to-noise ratio at ultra-high field MRI *Magnetic Resonance in Medicine* **85** 3522–30

Zhang B, Seifert A C, Kim J, Borrello J and Xu J 2017 7 Tesla 22-channel wrap-around coil array for cervical spinal cord and brainstem imaging *Mag. Reson. Med.* **78** 1623–34

Zhang X, Uğurbil K and Chen W 2001 Microstrip RF surface coil design for extremely high-field MRI and spectroscopy *Magnetic Resonance in Medicine* **46** 443–50

Zhao W, Cohen-Adad J, Polimeni J R, Keil B, Guerin B, Setsompop K, Serano P, Mareyam A, Hoecht P and Wald L L 2014 Nineteen-channel receive array and four-channel transmit array coil for cervical spinal cord imaging at 7T *Magnetic Resonance in Medicine* **72** 291–300

Zhu Y 2004 Parallel excitation with an array of transmit coils *Magnetic Resonance in Medicine* **51** 775–84